nature communications

Article

https://doi.org/10.1038/s41467-026-70911-4

CD8$^+$ T cells sustain vaccination-induced immunity against dissemination of contained tuberculosis in immunosuppressed hosts

Received: 10 June 2025

Accepted: 9 March 2026

Published online: 24 March 2026

Check for updates

Socorro Miranda-Hernandez[1], Manoharan Kumar[2,13], Alec Henderson[1,3,13], Erin Graham[4,13], Xiao Tan[5], Jim Taylor[6], Michael T. Meehan[1], Zuriel Ceja[7,8], Lidia del Pozo-Ramos[1], Yi Pan[9], Ellen Tsui[9], Meg L. Donovan[10], Miguel E. Rentería[7,8], Mario Alberto Flores-Valdez[11], Antje Blumenthal[10], Quan Nguyen[5], Selvakumar Subbian[12,14], Matt A. Field[2,6,14] & Andreas Kupz[1,14]

About two billion people are latently infected with *Mycobacterium tuberculosis* (*Mtb*), which can reside in multiple organs, including the lymphatics. The risk of latent *Mtb* infection (LTBI) reactivation increases with immunosuppression, such as HIV coinfection, yet the immunological correlates that maintain LTBI remain largely elusive. Using a mouse model of contained lymphatic *Mtb* infection we dissect the drivers of containment versus reactivation. We show that immunosuppression-induced dissemination of lymphatic *Mtb* and ensuing progressive disease can be prevented by vaccination with BCG or recombinant BCG even in the absence of CD4$^+$ T cells. Multi-parameter imaging, spatial transcriptomics and network analysis reveal that anti-CD4-mediated immunosuppression triggers distinct repositioning of non-CD4 immune cells at the edge of TB lesions in cervical lymph nodes. Although B cell numbers increase, they prove dispensable for *Mtb* containment during CD4$^+$ T cell loss. Using immune cell-deficient mice, cell depletion and adoptive transfers, we reveal that CD8$^+$ T cells mediate vaccination-induced prevention of *Mtb* dissemination in the absence of CD4$^+$ T cells, informing LTBI management in immunocompromised individuals.

Tuberculosis (TB), caused by *Mycobacterium tuberculosis* (*Mtb*), remains the leading infectious cause of death by a single pathogen globally, with about 1.3–1.5 million deaths annually. In addition, it is estimated that about two billion people are latently infected with *Mtb* without showing signs of active disease[1]. Latent *Mtb* infection (LTBI) is often contained within granulomatous lesions that can occur in multiple organs. However, immunosuppressed individuals often fail to control LTBI, and the risk of LTBI reactivation increases with human immunodeficiency virus (HIV) infection, type 2 diabetes, malnutrition, autoimmune diseases, and following organ transplantation[2,3]. While reinfection has been associated as the main driver of TB disease among individuals co-infected with HIV in high-TB burden countries[4], reactivation of LTBI appears to be a significant cause of disease in low burden countries[5]. A hallmark of HIV infection and several other immunosuppressive conditions is the impaired function and reduction or loss of CD4$^+$ T cells. These immune cells are crucial for TB control,

A full list of affiliations appears at the end of the paper. e-mail: andreas.kupz@jcu.edu.au

maintenance of the structural integrity of granulomas, and a primary target for vaccine-induced protection against TB[6,7]. However, due to the discrepancy between immunological parameters obtained in animal models and humans, the specific role of $CD4^+$ T cells in LTBI immunity is still debated, especially in immunocompromised individuals[8].

Recognising that LTBI shares common features with lymphatic diseases[9], we previously developed a mouse model to study LTBI reactivation following the loss of $CD4^+$ T cells[10]. This lymphocentric murine TB model, which involves ear dermis infection, reflects several immunological aspects of human LTBI. In this model, *Mtb* spreads to the lungs only in mice depleted of $CD4^+$ T cells after intradermal (i.d.) infection, while immunocompetent mice contain *Mtb* within the draining lymph nodes (LNs), mimicking aspects of LTBI. Historical descriptions of human TB and observations in non-human hosts suggest that TB has lymphatic characteristics, and that pulmonary pathology primarily aids disease transmission[9]. This lymphocentric view of TB is supported by findings that LNs, bone marrow, spleen, thymus, tonsils and adenoids are persistently infected with *Mtb* in humans and non-human primates and can serve as a source of LTBI reactivation[11–15]. In the absence of immunosuppression, this model mimics many of the immunological and cellular processes that are central to asymptomatic *Mtb* infection in humans[16]. While the infected cell types, the innate and adaptive immune responses, lymph node dissemination and *Mtb* replication dynamics are similar, the tissue microenvironment differs, and lung-specific pathology is minimal. For those reasons, the ear dermis infection model is increasingly recognized as a suitable tool to investigate immune responses associated with contained extrapulmonary *Mtb* infection[17,18].

Importantly, we have previously shown that Bacillus Calmette-Guérin (BCG) vaccination can prevent the dissemination of contained murine *Mtb* infection with anti-CD4 monoclonal antibodies (mAb), indicating that vaccine-induced $CD4^+$ T cells are not essential to prevent the spread of lymphatic murine LTBI[19]. This finding raised the fundamental question of which immune cells control *Mtb* containment within the lymphatics after BCG vaccination in the absence of $CD4^+$ T cells. Given the importance of managing and reducing LTBI to achieve the WHO's End TB Strategy[20], the contained murine lymphatic *Mtb* infection offers an opportunity to study LTBI reactivation from a lymphocentric perspective, and provides a valuable platform to explore the immunological requirements for LTBI containment versus dissemination in the context of vaccination. While macrophages and monocytes express CD4 in humans, they do not in mice[21]. This allows the study of $CD4^+$ T cell depletion in the presence of other immune cells, such as macrophages/monocytes. *Mtb* uses alveolar macrophages to disseminate, survive, and replicate; these cells are also critical to initiate the formation of granulomas[22,23]. Moreover, monocytes are altered in individuals with LTBI, so they may play a role in the reactivation of LTBI[24]. In this context, this mouse model selectively mimics the impaired function or loss of $CD4^+$ T cells in human LTBI.

Until recently, the dissection of the complex interactions between *Mtb* and the host immune system, which lead to the establishment of LTBI, predominantly relied on histopathological studies and cellular analyses of disrupted tissues or the extraction of DNA and RNA from blood. With the emergence of spatial tissue profiling in conjunction with multiplex imaging and advances in analytical methodologies, it is now possible to map and analyse the organisation and activity of thousands, or even millions, of cells, genes, and molecules in the tissue[25]. This approach has been used to map TB granulomas in the lungs, revealing the tissue architecture and cellular interactions in TB. It shows that *Mtb* infected human lung tissue comprises at least four types of non-necrotising structures in addition to necrotising granulomas[26]. Furthermore, spatial transcriptomics has provided unprecedented insights into the pathogenesis of Alzheimer's disease, Multiple Sclerosis, skin diseases and various types of cancers in different organs[27–30].

In this work, we employ a multi-pronged approach using several experimental strategies to dissect the immunological requirements of lymphatic LTBI containment. The first approach utilises histopathological and multi-parameter spatial transcriptomics techniques to delineate the LN architecture following lymphatic *Mtb* infection with and without prior vaccination with BCG or the recombinant BCG (rBCG) strain BCG::ESAT-6-PE25SS (abbreviated as PE25 in Figures) and assesses extrapulmonary organs for TB dissemination. In parallel, we perform *Mtb* infection and adoptive cell transfer in various mouse strains lacking distinct immune cell subsets and monitor their ability to resist *Mtb* spread. Our results give detailed high-dimensional insight into the cellular compositions during *Mtb* dissemination and BCG-mediated containment of *Mtb* in the lymphatics (Supplementary Fig. 1). Understanding the immune correlates of protective versus permissive host response has significant implications for designing preventative and therapeutic strategies to combat LTBI and its reactivation.

Results

BCG and BCG::ESAT-6-PE25SS vaccination prevent *Mtb* dissemination in a murine lymphatic LTBI model

Recombinant BCG strains have attracted considerable attention as potential substitutes for BCG[31,32]. We and others have developed candidate TB vaccines by integrating immunogenic proteins from the Region of Difference 1 (RD1) locus of *Mtb* into BCG. The first-generation rBCG strains containing RD1 from *Mtb* were considered inappropriate to progress to human trials due to prolonged persistence and increased virulence in immunocompromised hosts[33]. However, next-generation rBCG candidates, such as *Mtb*::$ESX1^{Mmar}$ and BCG::ESAT-6-PE25SS[34,35] aim to maintain the enhanced immunogenicity while preventing the detrimental aspects of *Mtb*-derived RD1. To enhance the likelihood of potential translation to clinical trials, it is important to evaluate rBCG strains in different pre-clinical models of TB.

To determine if BCG::ESAT-6-PE25SS can prevent the breakdown of contained lymphatic *Mtb* infection and the spread of *Mtb* to non-lymphatic organs, six- to eight-week-old C57BL/6 mice were grouped and treated as described in the Methods section and illustrated in Fig. 1a. Mice did not show clinical signs of active TB (Fig. 1b), and gained weight throughout the experiment (Fig. S2a-c).

Mice that only received *Mtb* infection contained the bacteria in the lymphatics (cervical lymph nodes (cLNs) and spleen) with negligible *Mtb* dissemination to the lungs (Fig. 1c-e). As previously shown[10,19], anti-CD4 mAb treatment led to a progressive increase in bacterial burden in LNs, spleens and lungs, with the most pronounced level of dissemination seen at 120 days after *Mtb* infection (Fig. 1c-e). While vaccination with BCG and BCG::ESAT-6-PE25SS did not reduce the level of *Mtb* bacilli in the lymphatic organs relative to anti-CD4 mAb-treated mice, it significantly reduced and, in some cases, BCG even prevented the spread of bacteria to the lungs (Fig. 1c-e). Apart from 2 animals that harboured a single colony of BCG in the lung or a single colony of BCG::ESAT-6-PE25SS in the spleen, all *Mtb*-uninfected control animals showed no detectable vaccine persistence in any of the organs at the 120-day time-point (Fig. 1f). Strikingly, when cervical LNs and lungs were assessed for histopathological changes by measuring the percent of tissue affected by *Mtb* (affected area, positive signal, magenta) in contrast with the unaffected area (normal in disease, negative signal, green) implementing an automated pixel function in QuPath (Fig. 1g, j), it became apparent that BCG and BCG::ESAT-6-PE25SS significantly reduced measurable pathology from day 30 onwards in the cLNs (Fig. 1h), and led to a significant reduction of lung pathology at 120 days after infection (Fig. 1k). Representative images show the area affected at 120 days after *Mtb* infection in cLNs and lungs

https://doi.org/10.1038/s41467-026-70911-4

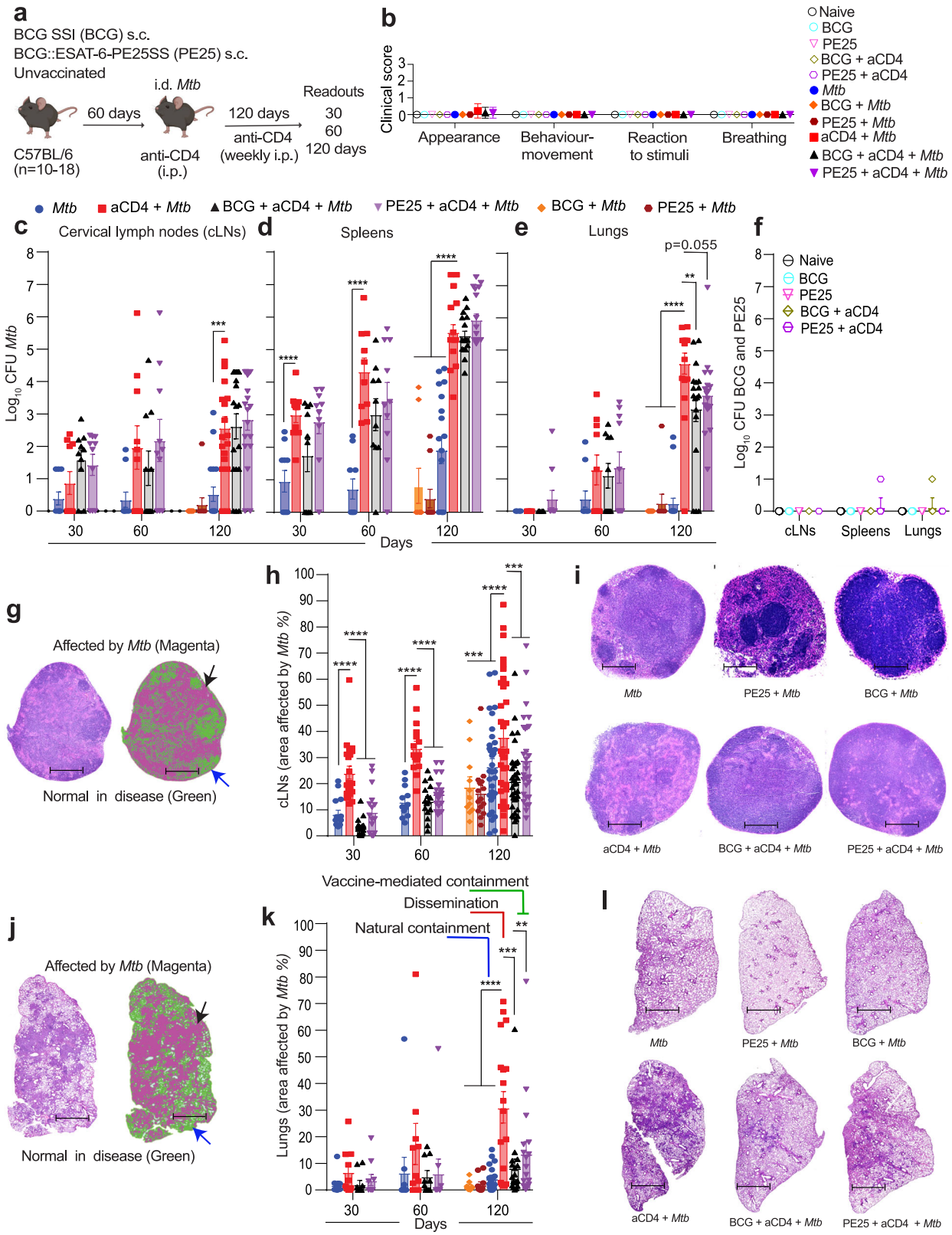

(Fig. 1i, l). Collectively, those results indicate that vaccination with BCG or BCG::ESAT-6-PE25SS significantly reduces the spread of *Mtb* from the lymphatic system to the lung and prevents the induction of lung pathology in this model of *Mtb* containment breakdown. Hence, for subsequent analyses we will refer to three distinct scenarios: i) natural containment (*Mtb* infection only); dissemination (*Mtb* infection plus anti-CD4 mAb treatment); and vaccine-mediated containment (vaccination with BCG or BCG::ESAT-6-PE25SS followed by *Mtb* infection and anti-CD4 mAb treatment) (illustrated in Fig. 1k).

Mtb dissemination occurs across multiple lymphatic and non-lymphatic organs

Given that TB can occur in multiple organs[36], we investigated whether reactivation of contained *Mtb* infection in our model impacts

Fig. 1 | BCG and BCG::ESAT-6-PE25SS vaccination prevent dissemination of contained *Mtb* infection following immunosuppression. a Experimental setup. C57BL/6 mice were vaccinated subcutaneously (s.c.) with 1×10^6 CFU of either BCG, BCG::ESAT-6-PE25SS (PE25) or left unvaccinated. Sixty days after vaccination, mice were infected intradermally (i.d). with 1×10^3 CFU of *Mtb* H37Rv. Some mice received anti-CD4 mAb (referred to in figure as aCD4) weekly intraperitoneally (i.p.) for 120 days. Groups without *Mtb* infection or anti-CD4 mAb treatment were included as controls. **b** Clinical scoring of disease ($n = 10$–18). **c**–**e** CFU of *Mtb* in (cLNs) ($n = 10$-18) (**c**), spleens ($n = 10$-18) (**d**), and lungs ($n = 10$–18) (**e**) at 30, 60 and 120 days post *Mtb* infection. **f** CFU of untreated (naïve), vaccination-only and uninfected and anti-CD4 mAb-treated controls in cLNs, spleens and lungs at 120 days ($n = 10$). **g**, **j** Representative H&E sections of cLNs (**g**) and lung left lobes (**j**) showing areas affected by *Mtb*. Normal tissue in disease (green; indicated by blue arrow) and areas affected by *Mtb* (magenta; indicated by black arrow). **h** Percent of tissue affected by *Mtb* in cLNs over time and representative H&E sections from each treatment group ($n = 10$–18). **k** Percent of tissue affected by *Mtb* in the left lung lobes over time indicating natural containment (blue), dissemination (red), and vaccine-mediated containment (green) ($n = 10$-18). **i**, **l** Representative H&E sections of cLNs (**i**) and left lung lobes (**l**) from each treatment group. Scale bars 0.14 μm. Results are presented as data means ± SEM (**b**), individual data points ± SEM (**c**–**f**, **h**, **k**) and representative images (**g**, **j**, **i**, **l**) from 3 pooled independent experiments with similar results ($n = 10$–18 mice per group). Statistical analyses: Two-way ANOVA followed by Tukey's multiple comparison test per time-point (one-sided) (**2b**–**f**), or One-way ANOVA followed by Kruskal-Wallis test with Dunn's multiple comparison test (one-sided) (**2h**–**k**); significant differences relative to the anti-CD4 mAb-treated group are shown and are indicated by asterisks: * $p_{HSD} < 0.05$, ** $p_{HSD\_PHT} < 0.01$ (**c**–**e**, and **k**), *** $p_{HSD\_PHT} < 0.001$ (**c**, **h**, **k**), **** $p_{HSD\_PHT} < 0.0001$ (**d**-**k**). Source data are provided as a Source Data file. The mouse icon is from BioRender. Kupz, A. (https://BioRender.com/65s841b).

additional lymphatic and non-lymphatic organs and whether vaccination can prevent this. To this end, histopathological analyses and automated scoring were conducted on mesenteric lymph nodes (mLNs), femurs, livers, brains, and salivary glands. Like in the cLNs (Fig. 1h), anti-CD4 mAb treatment led to significantly enhanced histopathology in mLNs from 60 days after *Mtb* infection. Vaccination with BCG and BCG::ESAT-6-PE25SS markedly and significantly reduced the level of mLN damage (Fig. 2a; Fig S3a). Histopathological changes in liver, femurs and bone marrow were also seen at different time points across anti-CD4 mAb and vaccination groups (Fig. 2b, c; Fig. S3b, c). No pathological changes were observed in either the brain or the salivary glands in any of the treatment groups at 120 days after infection (Fig. S3d). In line with these histopathological results, we also found significantly increased tissue area occupied by *Mtb* in the cLNs, the lungs, the mLNs, the livers, and the bone marrow of anti-CD4 mAb-treated animals using Ziehl-Neelsen staining (Fig. 2d). Both BCG strains significantly reduced this area in cLNs, lungs and mLNs to the level of *Mtb*-infected mice that did not receive anti-CD4 mAb treatment. Furthermore, BCG also significantly reduced the area occupied by *Mtb* in livers and bone marrows compared with *Mtb*-infected only mice, while the reduction seen with BCG::ESAT-6-PE25SS reached statistical significance in the liver. Collectively and consistent with data shown in Fig. 1, these results show that anti-CD4 mAb-mediated dissemination of LTBI occurs across multiple lymphatic organs, the lung and the liver, but not the brain or the salivary glands, and that vaccination can prevent this spread.

Containment of lymphatic LTBI is associated with changes in the composition and positioning of immune cells in the LNs

To determine the immunological mechanisms that may be associated with natural containment (*Mtb*-only) vs anti-CD4 mAb treatment-mediated dissemination vs vaccination-mediated containment (BCG or BCG::ESAT-6-PE25SS with anti-CD4 mAb) we first performed multiplex immunohistochemistry (IHC) in the entire cLNs and left lung lobes using eight fluorescent antibodies against CD3, CD4, CD8, B220, CD11b, CD11c, CD161c, *Mtb* and DAPI for the nuclei (Fig. 3a-d). Enumeration of single positive cell types across the whole cLNs confirmed an increase in *Mtb*-infected cells in the anti-CD4 mAb-treated group relative to the *Mtb*-only group and groups that received anti-CD4 mAb treatment but had been vaccinated prior with BCG or BCG::ESAT-6-PE25SS (Fig. 3e; Fig. S4a). In line with our previously published flow cytometry-based results[10,19], Multiplex IHC also confirmed the efficient depletion of $CD4^+$ cells in all groups that had received anti-CD4 mAb (Fig. 3e). Similar observations occurred when single positive cells of each marker were enumerated across the full lung lobes (Fig. S4b, c). Interestingly, anti-CD4 mAb treatment with or without prior vaccination led to a significant increase in B cells in the cLNs and a trend towards increased $CD8^+$ T cells in the lungs. Collectively, these analyses showed that there are numerical changes of distinct immune cell subsets in cLNs and lung that are either driven by *Mtb* infection, by anti-CD4 mAb treatment and/or by vaccination.

We subsequently extended the image analysis to determine cells positive for *Mtb* plus an additional cellular marker used in the multiplex IHC panel (Fig. 3f; and Fig. S4d). In both cLNs and lungs, *Mtb*-infected cells, including non-classical phagocytic and non-phagocytic subsets[37–39], were significantly increased in the anti-CD4 mAb-treated dissemination group across all the double-positive populations except Mtb^+CD8^+ in cLNs and Mtb^+B220^+ in the lungs (Fig. 3f; and Fig. S4d). In almost all double positive cell populations across cLNs and lungs, the vaccinated groups showed a similar profile to the *Mtb*-only group. The only combination where all groups showed near-identical cellular abundance were Mtb^+CD8^+ cells in the cLN. Collectively, these results correlated with the increased *Mtb* burden observed in the anti-CD4 mAb-treated group with CFU plating (Fig. 1c, e), H&E (Fig. 1h, k) and ZN histopathology (Fig. 2d). The findings suggest that control of lymphatic LTBI through vaccination may be linked to changes in migration, abundance or functionality of B cells or $CD8^+$ T cells.

To measure if *Mtb* containment is also associated with an altered immune cell localisation around *Mtb*-infected cells, we performed proximity measurements. To this end, the distance of over 13 million cells expressing one of eight different markers in relation to *Mtb*-infected cells was analysed across cLNs and lungs (Fig. 3g, h; and Fig. S4e, f). In cLNs, a noticeable shift of all single-positive cells towards *Mtb*-infected cells in the anti-CD4 mAb-treated dissemination group was observed (Fig. 3g). As a general pattern in the cLNs, the *Mtb*-only group (blue) and the BCG-vaccinated group (black) showed similar cellular distances from *Mtb*-infected cells across most cell types, except $CD8^+$ and $CD11c^+$ cells (Fig. 3h). Likewise, the anti-CD4 mAb-treated group (red) clustered together with the BCG::ESAT-6-PE25SS-vaccinated group (purple) across the same cell types (Fig. 3h). $CD11c^+$ cells were the closest cell type to *Mtb*-infected cells in all anti-CD4 mAb-treated groups (Fig. 3g). Even though $CD8^+$ cell proportions did not increase in the LNs following anti-CD4 mAb treatment (Fig. 3e) they showed a consistent pattern of a similarly short distance from *Mtb*-infected cells in all anti-CD4 mAb treated groups (Fig. 3g, h). Despite increasing in relative abundance (Fig. 3e), $B220^+$ cells showed the largest distance to *Mtb*-infected cells in all groups (Fig. 3g, h). In the lungs, like the cLNs, there was a noticeable and highly significant shift towards *Mtb*-infected cells in all single-positive cells within the anti-CD4 mAb dissemination group (red) (Fig. S4e, f).

When taking into account abundance (Fig. 3e, f; and Fig. S4c, d) and distance measurement (Fig. 3g, h; and Fig. S4e, f), it appears that natural- and BCG-mediated containment of lymphatic LTBI may be linked to an influx and a repositioning of immune cells in the infected cLNs and the lungs. In particular, $B220^+$ B cells increased in the cLNs, and maintained the largest distance to *Mtb*-infected cells; $CD8^+$ T cells showed a reduced distance to *Mtb*; and $CD161c^+$ NK cells tightly clustered around *Mtb*-infected cells in lung tissue.

https://doi.org/10.1038/s41467-026-70911-4

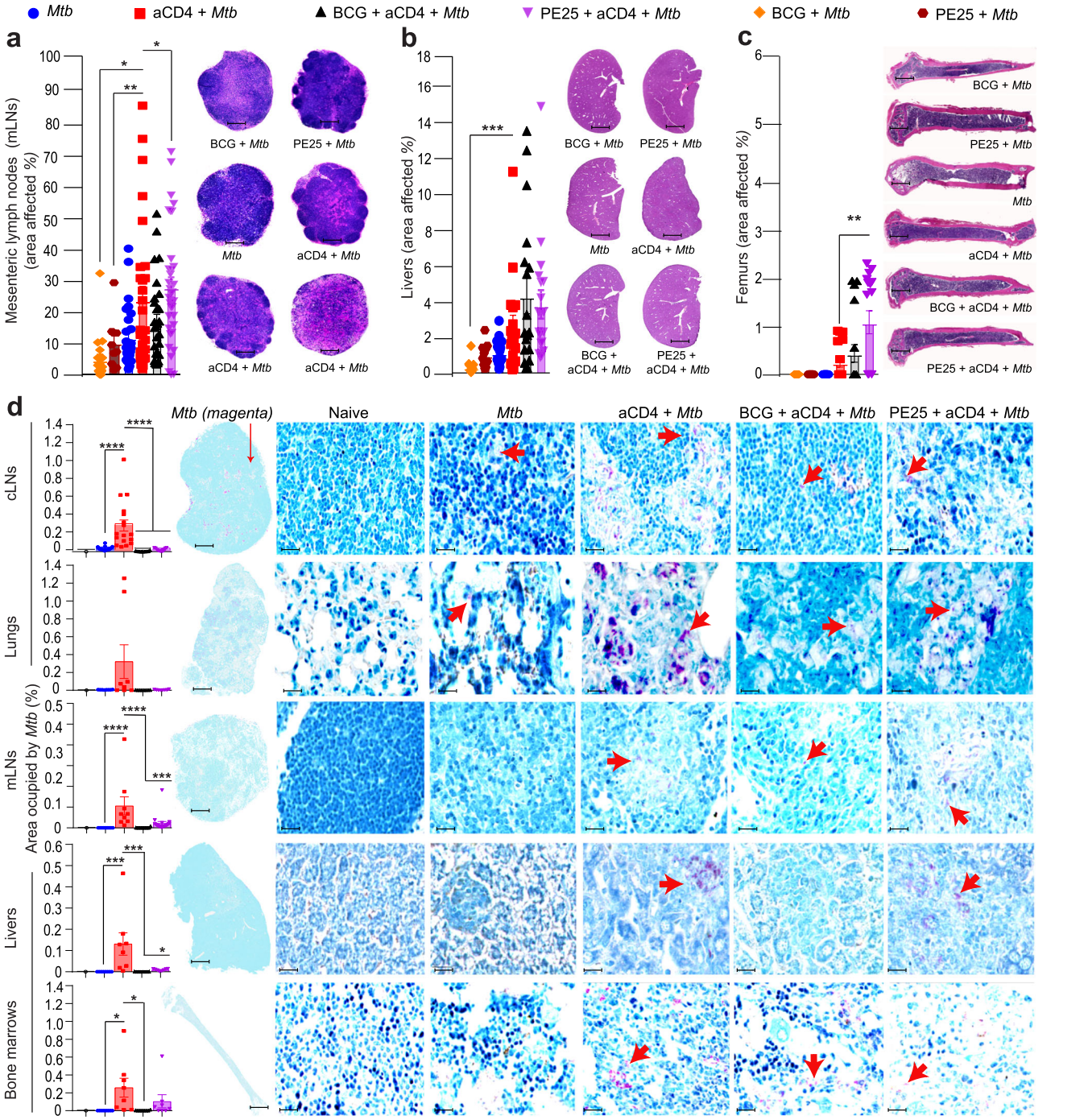

Fig. 2 | *Mtb* dissemination occurs across multiple lymphatic and non-lymphatic organs. a–c Percent of tissue affected by *Mtb* in mLNs (derived from 18 mice per group) (**a**), livers (derived from 18 mice per group) (**b**), and femurs (derived from 18 mice per group) (**c**) over time, including a representative H&E-stained section of each tissue from different treatment groups. **d** Percentage of the area occupied by *Mtb* in cLNs, lungs, mLNs, livers, and bone marrows with representative sections stained with Ziehl-Neelsen (ZN) ($n = 8$). Bacteria are shown in magenta and indicated with red arrows. Scale bars 0.14 μm and 0.093 μm. Results are presented as individual data points ± SEM (**a**–**d**) and representative images from 3 pooled independent experiments with similar results ($n = 8$–18 mice per group). Statistical analyses: One-way ANOVA followed by Kruskal-Wallis test with Dunn's multiple comparison test or Ordinary One-way ANOVA with Dunnett's multiple comparison test (both one-sided); significant differences relative to the anti-CD4 mAb-treated group are shown and are indicated by asterisks: * $p_{PHT} < 0.05$ (**a**, **d**), ** $p_{PHT} < 0.01$ (**a**, **c**), *** $p_{PHT} < 0.001$ (**b**, **d**), **** $p_{PHT} < 0.0001$ (**d**). Source data are provided as a Source Data file.

Spatial transcriptomics reveals distinct pathways of LTBI containment and dissemination at the edge of LN lesions

To assess whether anti-CD4 mAb-mediated *Mtb* dissemination and vaccine-mediated containment are associated with distinct transcriptomics signatures within defined regions of the cLNs, we performed NanoString GeoMx-based spatial transcriptomics across 30 regions of interest (ROIs) that were selected within normal tissue (in both naïve and disease samples) taken either from the lesion or the edge of a lesion of the cLNs across all groups (Fig. 4a, b). A UMAP analysis revealed some clustering of ROIs based on both tissue location and treatment group (Fig. 4c). We performed differentially expressed genes (DEGs) analysis observing significant differences between ROIs

https://doi.org/10.1038/s41467-026-70911-4

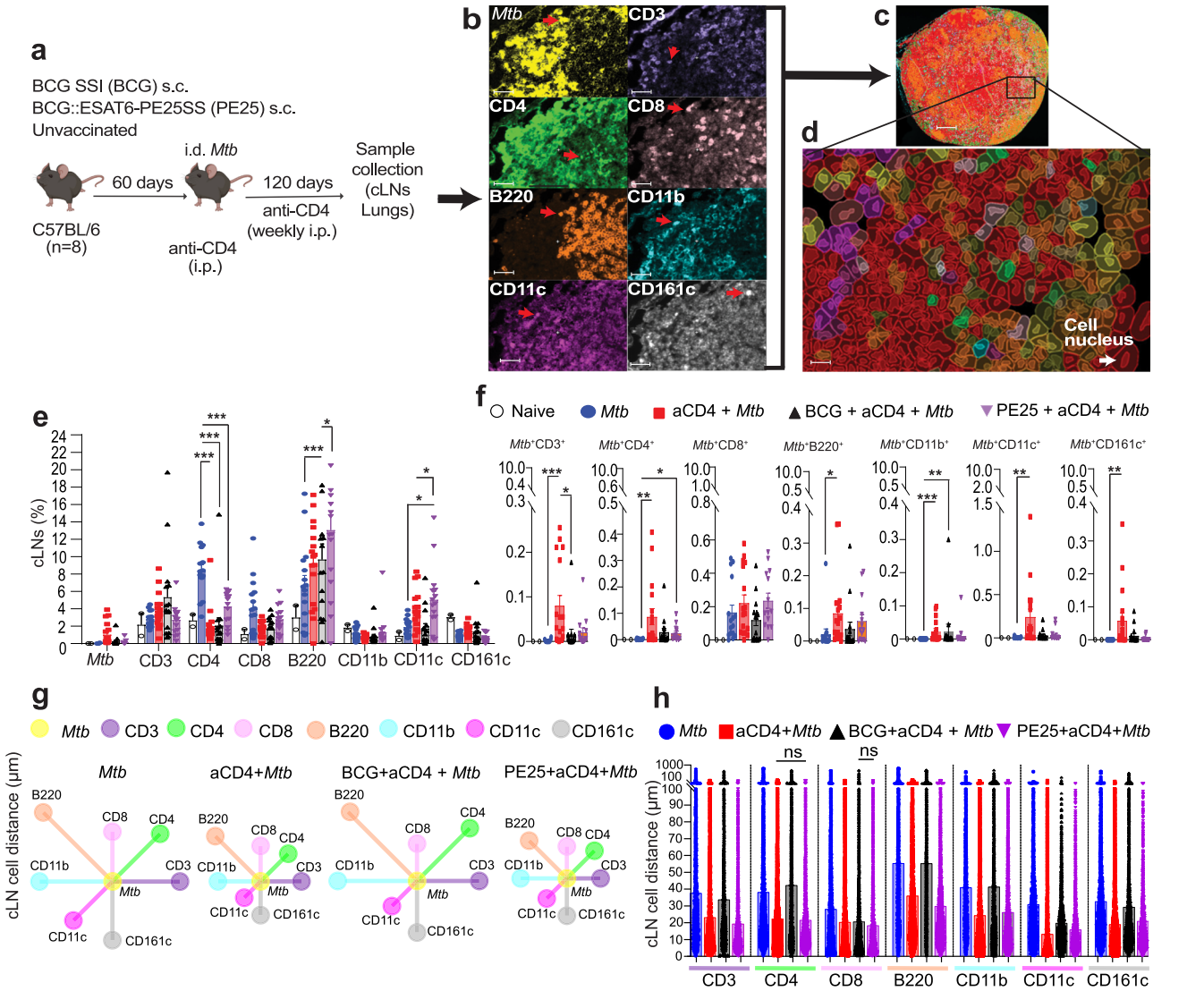

Fig. 3 | BCG vaccination increases B cell abundance and alters cellular positioning around *Mtb*-infected cells. a Experimental setup. **b** Representative images of Opal multiplex immunohistochemistry obtained from cLNs. A characteristic cell type is indicated with red arrows. **c** Representative cLN image after classifying each cell type with its respective marker. Black arrows indicate the sequence of the steps. **d** Enlarged area delineating the cells and nucleus of each cell, coloured according to the markers expressed within them: *Mtb* (yellow), CD3 (purple), CD4 (green), CD8 (pink), B220 (orange), CD11b (cyan), CD11c (magenta) and CD161c (white). **e** Percentage of single positive cells across entire cLNs ($n = 8$). **f** Proportion of cells positive for *Mtb* plus an additional cellular marker in cLNs ($n = 8$). **g**, **h** Schematic (**g**) and bar diagram (**h**) of the mean distance in micrometres of CD3, CD4, CD8, B220, CD11b, CD11c or CD161c positive cells to *Mtb* infected cells in cLNs ($n = 8$). Results are presented as individual data points ± SEM (**e**, **f**, **h**) and representative images (**b**–**d**) and distance plots (**g**) from 2-14 LNs derived from 2 independent experiments at 120 days after *Mtb* infection with similar results ($n = 8$ mice per experimental group; 2 naïve controls). Scale bars 0.14 µm and 0.093 µm. Statistical analyses: One-way ANOVA followed by Kruskal-Wallis test with Dunn's multiple comparison test or Two-way ANOVA followed by Tukey's multiple comparison test (both one-sided) per cell type; significant differences relative to the anti-CD4 mAb-treated group are shown and are indicated by asterisks: * $p_{HSD\_PHT} < 0.05$ (**e**, **f**), ** $p_{PHT} < 0.01$ (**f**), *** $p_{HSD\_PHT} < 0.001$ (**e**, **f**, **h**), **** $p_{PHT} < 0.0001$(**h**). See also Supplementary Fig. 4. Source data are provided as a Source Data file. The mouse icon is from BioRender. Kupz, A. (https://BioRender.com/65s841b).

derived from all tissue locations (Fig. 4d). Despite many observed differences, comparing all 30 ROIs independently of tissue location identified no significant DEGs between *Mtb* infection and anti-CD4 mAb-mediated dissemination relative to naïve mice (Fig. S5a). Significant differences were however observed in three comparisons: separated naïve tissue vs natural containment (*Mtb* only) (Fig. S5b), natural containment vs anti-CD4 mAb-mediated dissemination (Fig. S5c) and anti-CD4 mAb-mediated dissemination vs vaccine-mediated containment (Fig. S5d, e). Pathway analysis of DE genes using Ingenuity Pathway Analysis (IPA) revealed that many immune system-related pathways were enriched with a predicted activation (Fig. S5f, g). Overall, the anti-CD4 mAb dissemination group vs *Mtb*-only group showed the largest difference followed by both vaccination groups, illustrating key differences between dissemination and containment of LTBI on a transcriptional level. MHC-I-mediated antigen presentation and B cell receptor signalling were identified in the most highly significant pathways differentiating LTBI containment from anti-CD4 mAb-mediated dissemination (Figs. S5f, g). Strikingly, this aligned with our observations that B cells and CD8 cell numbers and distribution respectively were altered following anti-CD4-mediated dissemination of LTBI (Fig. 3),

When natural containment (*Mtb* only), dissemination (anti-CD4) and vaccination-mediated containment (BCG/PE25) were compared across ROIs derived from normal tissue, few DEGs were up- or down-regulated (Fig. 4e). In contrast, we observed many significant DEGs between natural containment, anti-CD4 mAb-mediated dissemination

https://doi.org/10.1038/s41467-026-70911-4

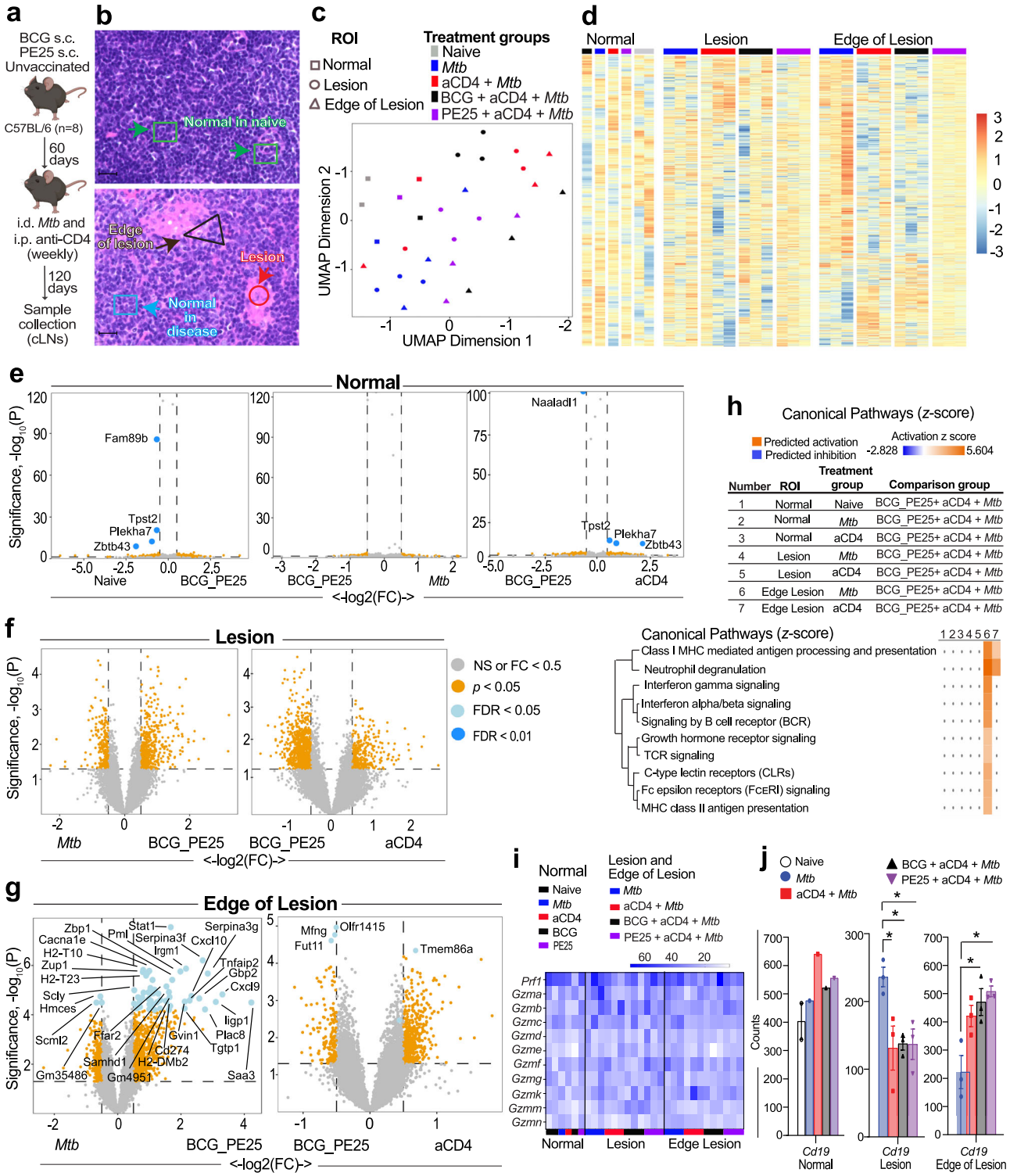

and vaccine-mediated containment within the lesion and at the edge of a lesion (Fig. 4f, g). Notably, most significant DEGs (FDR < 0.05 light blue; <0.01 dark blue) were identified at the edge of a lesion rather than within the lesion, particularly when comparing natural with vaccination-mediated containment (Fig. 4f, g). Interestingly, many immune-cell related pathways, including neutrophil degranulation and T and B cell-associated pathways were all strongly enriched when comparing the edge of the lesion in natural containment vs vaccination-mediated containment (Fig. 4g, h). Likewise, MHC-I-mediated antigen presentation and neutrophil degranulation differentiated the edge of the lesion in anti-CD4 mAb dissemination from vaccine-mediated containment. While neutrophil degranulation is likely a response to bacterial burden[40] and neutrophil swarming[41], T and B cell signatures support the findings from the multiplex IHC analysis (Fig. 3). The expression of cytotoxic genes was not statistically different between treatment groups and tissue types, possibly due to the lack of single cell resolution with NanoString GeoMx (Fig. 4i).

Using NanoStringNCTools to assign cell types (Fig. 4j; and Fig. S6a–f), we observed significant changes in the proportions of B cells (*Cd19*), CD4 cells (*Cd4*), dendritic cells (*Itgax*), and NK cells (*Klrblc*), again in accordance with our key findings from the multiplex IHC analysis (Fig. 3). These changes largely distinguished natural LTBI

Fig. 4 | Dissemination and containment of LTBI are associated with respective transcriptional changes at the edge of lesions. NanoString GeoMx spatial transcriptomics results were derived from 30 ROIs. **a** Experimental setup. **b** Representative H&E-stained sections from cLNs. Arrows indicate the different ROI types used in the study. Normal in naïve (green) and during disease (blue), lesion (red), and edge of the lesion (black). **c** UMAP analyses show clustering of ROIs based on tissue type and treatment group. **d** Heatmap showing DEGs across the different ROIs and treatment groups. **e**–**g** Volcano plots showing the comparisons of the ROIs in normal (**e**) ($n = 2$), lesion (**f**) ($n = 8$) and edge of the lesion ($n = 8$) (**g**) across the treatment groups relative to the combined vaccines BCG and PE25. **h** Immune system-related IPA pathways considering activation or inhibition (z-scores) across ROIs in the treatment groups ($n = 8$). **i** Heatmap showing expression of cytotoxic genes across tissue types and treatment groups ($n = 8$). **j** Gene transcript-based cellular deconvolution with estimated counts of *Cd19* positive cells depending on the ROI in normal tissue, the lesion, and the edge of lesions ($n = 8$). Results are presented as heatmaps (**d**, **i**, **j**), volcano plots (**e**–**g**), representative images (**b**) and bar graphs ± SEM (**h**) from 2-14 cLNs derived from 2 independent experiments with similar results at 120 days after *Mtb* infection ($n = 8$ mice per experimental group; 2 naïve controls). Scale bars 0.093 μm. Statistical significance of differential expressed genes using following cut-off: false discovery rate (FDR) < 0.05 (two-sided). e-g, and Fisher's exact test (one-sided) for (**h**, **i**) as described in Methods; (**j**) Two-way ANOVA followed by Tukey's multiple comparison test (one-sided); significant differences relative to the *Mtb*-only group and among treatment groups are shown and are indicated by asterisks. * $p_{FDR,HSD,FET} < 0.05$ (**e**, **f**, **h**, **I**, **j**),. See also Figs. S5–S6. Source data are provided as a Source Data file. The mouse icon is from BioRender. Kupz, A. (https://BioRender.com/65s841b).

containment from anti-CD4 mAb treatment (Fig. 4j, i; and Fig. S6a–f). Consistently, cell changes were most pronounced at the edge of the lesion (Fig. S6b, c). Most notably, the overall increase in B cells following anti-CD4 mAb treatment (previously observed by multiplex IHC) was localised to the edge of the lesion and further associated with a marked decline of *Cd19* within the lesion (Fig. 4j).

Differences in cytokine (Fig. S6g–i) and chemokine (Fig. S6j–l) gene expression were also observed within the lesion and their edges. While in some cases increased cytokine or chemokine expression was only seen in the anti-CD4 mAb dissemination group (lesion / edge of lesion: *Il1a, Il1b, Il18* and lesion only *Ifnγ*, *Tnf, Cxcl10, Cxcl13*), likely reflecting the increased inflammation associated with higher bacterial burden, some cytokines/chemokines increased with anti-CD4 mAb treatment more broadly (lesion: *Ccl2, Ccl4, Cxcl9*; edge of lesion: *Tnf, Ccl2, Ccl5, Ccl19, Cxcl9, Cxcl10, Cxcl13*) or were increased with containment (lesion: *Ccl5, Ccl21a*; edge of lesion: *Ifnb1, Ccl22*).

Collectively, these results support significant repositioning of immune cells in cLNs in response to vaccination and depletion of $CD4^+$ T cells and revealed that transcriptomic changes associated with dissemination and containment of lymphatic LTBI are predominantly localised at the edge of a lymphatic lesion.

Lethal dissemination of *Mtb* occurs in the combined absence of lymphocytes and is independent of innate responses

Cumulatively, our analyses thus far inferred that lymphatic LTBI containment may be associated with an expansion and/or repositioning of immune cells, particularly B cells, $CD8^+$ T cells and NK cells at the edge of the cLN lesions. To experimentally address the role of these cells for lymphatic LTBI containment, we induced lymphatic *Mtb* infection in a variety of genetically modified mouse strains with and without vaccination. First, we infected wild-type C57BL/6 mice, B6.*muMT*$^{-/-}$ mice that lack mature B cells[42], B6.*Rag1*$^{-/-}$ mice that lack mature B and T cells[43] and B6.*Rag2*$^{-/-}$*Il2rg*$^{-/-}$ mice that lack mature B, T and NK cells[44] i.d. with *Mtb*. Two groups of C57BL/6 mice received anti-CD4 mAb treatment either alone or in addition to *Mtb* infection and naïve mice were also included as controls (Fig. 5a). While all C57BL/6 mice and all B6.*muMT*$^{-/-}$ mice survived *Mtb* infection for 120 days (Fig. 5b, c), 100 % of infected *Rag1*$^{-/-}$ mice succumbed to the infection with a median survival of 71 days (Fig. 5d). Severely immunocompromised B6.*Rag2*$^{-/-}$*Il2rg*$^{-/-}$ mice only survived for an average of 56 days (Fig. 5e). These results indicated that the absence of $CD4^+$ T cells or B cells alone does not lead to death, whereas the combined absence of B and T cells does. The results also implied that NK cells may play a minor contribution to LTBI containment in the absence of B and T cells. As expected, and in line with results reported in Fig. 1, anti-CD4 mAb-treated C57BL/6, B6.*Rag1*$^{-/-}$ and B6.*Rag2*$^{-/-}$*Il2rg*$^{-/-}$ mice also showed high levels of CFU in the cLNs, lung and spleen (Fig. 5h) as well as significantly elevated histopathological damage in cLNs (Fig. 5i, j) and lungs (Fig. 5k, l). However, when we enumerated the *Mtb* burden in surviving C57BL/6 and B6.*muMT*$^{-/-}$ mice, we were intrigued to observe that B6.*muMT*$^{-/-}$ mice showed almost no signs of bacterial spread nor a productive infection in the lymphatics (Fig. 5f–l). RNA sequencing of fixed cLNs also revealed that the transcriptomic response of B6.*muMT*$^{-/-}$ mice to lymphatic *Mtb* infection differed from C57BL/6 as well as from immunocompromised B6.*Rag1*$^{-/-}$ and B6.*Rag2*$^{-/-}$*Il2rg*$^{-/-}$ mice (Fig. 5m). Furthermore, pathway analysis of RNAseq data revealed that severe infection in immunocompromised B6.*Rag1*$^{-/-}$ and B6.*Rag2*$^{-/-}$*Il2rg*$^{-/-}$ mice and anti-CD4 mAb-treated C57BL/6 mice is associated with a particularly strong neutrophil degranulation signature relative to B6.*muMT*$^{-/-}$ mice. Instead, *Mtb*-infected B6.*muMT*$^{-/-}$ mice were associated with class I MHC-mediated antigen processing and presentation (Fig. S7a, b).

We reasoned that if BCG vaccination-mediated containment of LTBI was driven by innate immune mechanisms, then vaccination of B6.*Rag1*$^{-/-}$ or B6.*Rag2*$^{-/-}$*Il2rg*$^{-/-}$ mice before *Mtb* infection should extend their survival (Fig. 5o). However, vaccination with BCG or BCG::ESAT-6-PE25SS did not extend the survival of B6.*Rag1*$^{-/-}$ mice (Fig. 5r) and only marginally extended the survival of B6.*Rag2*$^{-/-}$*Il2rg*$^{-/-}$ mice (Fig. 5s). Also, vaccination did not change the survival of B6.*muMT*$^{-/-}$ or C57BL/6 mice (Fig. 5p, q). Collectively, these results indicated that prevention of severe disease and death after *Mtb* dissemination may either be driven by B and T cell interactions or by a compensatory effect of $CD8^+$ T cells. The results also demonstrated that vaccine-mediated LTBI containment is likely driven by adaptive immune responses with only a minor contribution of innate immunity in the absence of adaptive immune cells (e.g., T/B cell-dependent innate training).

$CD8^+$ T cells mediate LTBI containment following anti-CD4 mAb treatment and B cells are dispensable

Next, we wanted to further quantify the relative contributions of B cells and different T cell subsets in the containment of LTBI. For this, we first established an adoptive transfer system that would allow us to dissect the contributions of cell subsets on mouse survival (Fig. 6a). We confirmed that adoptive transfer of LN- or spleen-derived cells from wild type C57BL/6 mice into B6.*Rag2*$^{-/-}$*Il2rg*$^{-/-}$ mice can reverse the 100% mortality observed after *Mtb* infection into 100% survival (Fig. 6b). This provided a tractable system to transfer LN cells that were depleted of either T cells, B cells or both (Fig. 6c). Almost all mice that received total LN cells, regardless of whether cells came from naïve or vaccinated donors, survived for 120 days (Fig. 6d). In line with the results seen in B6.*muMT*$^{-/-}$ mice, the survival data clearly showed that the absence of B cells from transferred cells can be compensated for, with 100% of mice that received cells from B cell depleted vaccinated animals surviving for 120 days and ~70% of mice that received cells from B cell depleted naïve mice surviving for 120 days (Fig. 6e). In contrast, mice that received either $CD3^+$ (Fig. 6f) or $CD3^+$ and $CD19^+$ cell-depleted LN cells (Fig. 6g) succumbed to the dissemination of *Mtb* infection between 40 and 80 days, which was indistinguishable from B6.*Rag2*$^{-/-}$*Il2rg*$^{-/-}$ mice that had received no cells. These results mirrored the survival data seen in B6.*Rag1*$^{-/-}$ mice (Fig. 6d) but pointed towards a critical role for T cells rather than B cells in mediating LTBI containment.

Given that vaccination prevented dissemination and pathology despite the depletion of $CD4^+$ cells (Fig. 1), the most likely explanation

https://doi.org/10.1038/s41467-026-70911-4

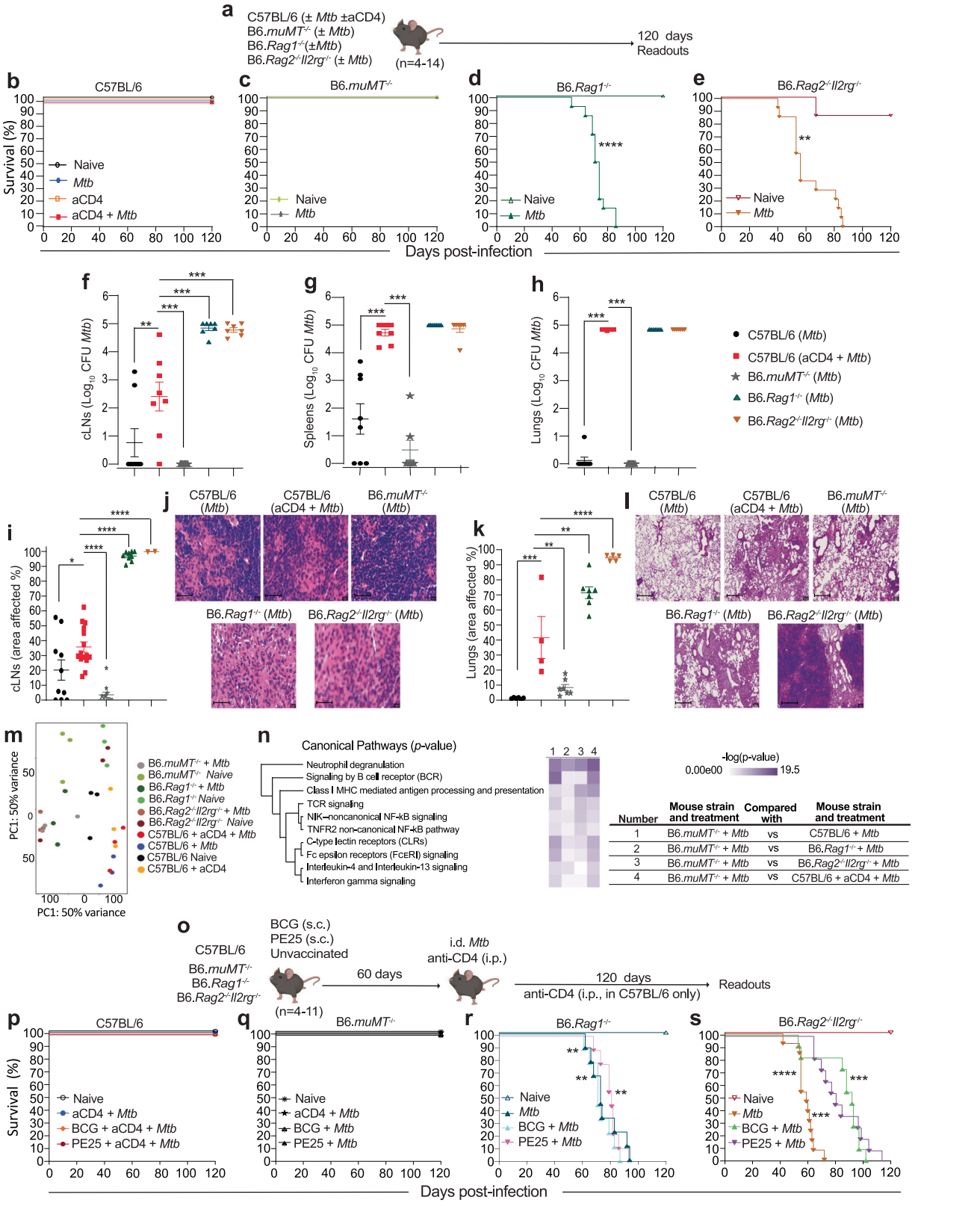

for the results obtained above, was that containment of lymphatic *Mtb* is mediated by $CD8^+$ T cells. To definitively assess the relative contributions of $CD4^+$ T cells, $CD8^+$ T cells and B cells to the prevention of lethal *Mtb* dissemination, we performed additional experiments in which C57BL/6 wild-type mice and B cell-deficient B6.*muMT*$^{-/-}$ mice were vaccinated or left unvaccinated and were subsequently treated with anti-CD4 mAb, anti-CD8 mAb or both (Fig. 6h). Both vaccine strains induced TB10.4:H-$2K^{b+}$ mycobacteria-specific $CD8^+$ T cells, including in the cLNs (Fig. 6i). Strikingly, in both genetic backgrounds only mice treated with both anti-CD4 and anti-CD8 mAbs succumbed to the infection (Fig. 6j), with similar kinetics to B6.*Rag1*$^{-/-}$ mice (Fig. 6d) and B6.*Rag2*$^{-/-}$*Il2rg*$^{-/-}$ mice that had received T cell-depleted LN cells (Fig. 6e). While the overall dependency on $CD8^+$ T cells for survival in the absence of $CD4^+$ T cells was identical between unvaccinated and

Fig. 5 | Lethal *Mtb* dissemination occurs in the combined absence of lymphocytes and is independent of innate responses. a Experimental setup of unvaccinated mice. **b**–**e** Percent survival of C57BL/6 (Naïve $n = 6$, *Mtb* $n = 14$, aCD4 $n = 4$, aCD4+*Mtb* $n = 12$) (**b**), B6.*muMT*$^{-/-}$ (Naïve $n = 7$, *Mtb* $n = 14$) (**c**), B6.*Rag1*$^{-/-}$ (Naïve $n = 5$, *Mtb* $n = 14$) (**d**), and B6.*Rag2*$^{-/-}$*Il2rg*$^{-/-}$ (Naïve $n = 7$, *Mtb* $n = 14$) (**e**), mice following i.d. infection with *Mtb* and anti-CD4 mAb treatment (C57BL/6 only; (**b**). **f**–**h** *Mtb* CFU burden in cLNs (C57BL/6+*Mtb* $n = 8$, C57BL/6+aCD4+*Mtb* $n = 8$, B6.*muMT*$^{-/-}$+*Mtb* $n = 7$, B6.*Rag1*$^{-/-}$+*Mtb* $n = 7$, B6.*Rag2*$^{-/-}$*Il2rg*$^{-/-}$+*Mtb* $n = 7$) (**f**), spleens (C57BL/6+*Mtb* $n = 8$, C57BL/6+aCD4+*Mtb* $n = 8$, B6.*muMT*$^{-/-}$+*Mtb* $n = 7$, B6.*Rag1*$^{-/-}$+*Mtb* $n = 7$, B6.*Rag2*$^{-/-}$*Il2rg*$^{-/-}$+*Mtb* $n = 7$) (**g**), and left lung lobes (C57BL/6+*Mtb* $n = 8$, C57BL/6+aCD4+*Mtb* $n = 8$, B6.*muMT*$^{-/-}$+*Mtb* $n = 7$, B6.*Rag1*$^{-/-}$+*Mtb* $n = 7$, B6.*Rag2*$^{-/-}$*Il2rg*$^{-/-}$+*Mtb* $n = 7$) (**h**) at the time of euthanasia or at 120 days after *Mtb* infection for surviving mice. Percent of tissue affected by *Mtb* in cLNs (C57BL/6+*Mtb* $n = 8$, C57BL/6 + aCD4+*Mtb* $n = 8$, B6.*muMT*$^{-/-}$+*Mtb* $n = 7$, B6.*Rag1*$^{-/-}$+*Mtb* $n = 7$, B6.*Rag2*$^{-/-}$*Il2rg*$^{-/-}$+*Mtb* $n = 7$) (**i**) and left lobe lungs (C57BL/6+*Mtb* $n = 8$, C57BL/6+aCD4+*Mtb* $n = 8$, B6.*muMT*$^{-/-}$+*Mtb* $n = 7$, B6.*Rag1*$^{-/-}$+*Mtb* $n = 7$, B6.*Rag2*$^{-/-}$*Il2rg*$^{-/-}$+*Mtb* $n = 7$) (**k**). Representative H&E sections of cLNs (**j**) and left lung lobes (**l**). Scale bars 0.14 μm. **m**, **n** Bulk-RNA sequencing results obtained from paraffin-embedded cLN sections. **m** PCA plot of RNAseq of wild-type, anti-CD4 mAb immunosuppressed, and mutant mice. **n** IPA pathway analysis comparing cLNs between *Mtb*-infected B6. B6.*muMT*$^{-/-}$ mice and other groups. **o** Experimental setup of mice following i.d. infection with *Mtb* and prior vaccination with BCG or PE25. **p**–**s** Percent survival of C57BL/6 (Naïve $n = 8$, aCD4+*Mtb* $n = 6$, BCG+aCD4+*Mtb* $n = 6$, PE25+aCD4+*Mtb* $n = 7$) (**p**), B6.*muMT*$^{-/-}$ (Naïve $n = 7$, aCD4+*Mtb* $n = 6$, BCG+*Mtb* $n = 5$, PE25+*Mtb* $n = 5$) (**q**), B6.*Rag1*$^{-/-}$ (Naïve $n = 4$, *Mtb* $n = 9$, BCG+*Mtb* $n = 9$, PE25+*Mtb* $n = 9$) (**r**), and B6.*Rag2*$^{-/-}$*Il2rg*$^{-/-}$ (Naïve $n = 10$, *Mtb* $n = 13$, BCG+*Mtb* $n = 11$, PE25+*Mtb* $n = 11$) (**s**). Results are presented as individual data points ± SEM (**f**–**i**, **k**), representative H&E images (**j**, **l**), and Long-rank (Mantel-Cox) test (two-sided) for survival curves (**b**–**e**, **p**–**s**). Scale bars 0.093 μm. Data pooled from 2-3 independent experiments with similar results ($n = 5$–16 mice per experimental group). Statistical analyses: One-way ANOVA followed by Tukey's multiple comparison test (one sided) (**f**–**i**, **k**), Fisher's exact test (one-sided) and Long-rank (Mantel-Cox) test for survival curves (two-sided) **(b-e, p-s)**. Significant differences are indicated by lines and asterisks: * $p_{PHT\_FET} < 0.05$ _ (**i**, **n**), ** $p_{HSD\_PHT} < 0.01$ (**e**, **f**, **k**, **r**), *** $p_{HSD\_PHT} < 0.001$ (**g**, **h**, **k**, **s**), **** $p_{HSD\_PHT} < 0.0001$ (**d**, **I**, **k**, **s**). See also Figure S7. Source data are provided as a Source Data file. The mouse icon is from BioRender. Kupz, A. (https://BioRender.com/65s841b).

vaccinated mice, as expected, vaccinated anti-CD4/CD8 mAb-treated mice showed a survival increase of ~20–30 days compared to unvaccinated mice (Fig. 6j). In line with the survival data, the CFU results show that CD8$^+$ T cell depletion by itself does not lead to dissemination of latent *Mtb* infection to the lung (Fig. 6k, l). However, combined CD4/CD8 T cell depletion leads to dissemination of contained *Mtb* infection. Following vaccination, two anti-CD4/CD8 mAb-treated C57BL/6 mice survived until day 120. While these two mice had reached an ethical endpoint, organs could be collected prior to euthanasia. As expected, very high *Mtb* CFU were recovered from cLNs, spleen and lungs of those two mice. Taken together, our results clearly demonstrate that LTBI containment is driven by T cells and that B cells are dispensable for this process (Fig. 6j, k). While the absence of either CD4$^+$ or CD8$^+$ T cells can be compensated for, regardless of whether B cells are present or not (C57BL/6 vs B6.*muMT*$^{-/-}$), the combined absence of both CD4$^+$ and CD8$^+$ T cells was always lethal. Our results also show that NK cells alone cannot compensate for the loss of T cells (Fig. 6m).

Collectively, our data provide a comprehensive assessment of the cellular requirements for the lymphatic containment of otherwise fatal *Mtb* dissemination and provide strong evidence that CD8$^+$ T cell-mediated immunity should be targeted to avoid LTBI reactivation when CD4$^+$ T cell immunity is compromised, such as in the context of HIV co-infection.

Discussion

Despite the availability of a licensed vaccine for over 100 years, TB still claims over a million lives per year, and it is widely accepted that a lack of clear immunological correlates of protection has prevented the development of a better TB vaccine[45]. Hence, identifying such correlates represents the 'holy grail' in TB research. Given that a proportion of active TB is a consequence of reactivated LTBI[46], understanding the mechanisms that control *Mtb* containment will likely contribute to the development of an improved vaccine and potential immunotherapeutic approaches for LTBI.

Here, we provide compelling evidence that contained lymphatic infection of *Mtb* is exclusively maintained by hierarchical and redundant contributions of T cells. While deficiency in either CD4$^+$ T cells or CD8$^+$ T cells led to a slow but progressive dissemination of *Mtb*, rapid and lethal *Mtb* spread only occurred in the absence of both T cell subsets. In contrast, our results show that CD4$^+$ and CD8$^+$ T cell deficiency could not be compensated for by B cells and that B cells are not required for lymphatic containment in this model of LTBI. These findings provide detailed insights into the reactivation dynamics of LTBI and provide concrete evidence that CD8$^+$ T cells are sufficient to control lymphatic *Mtb* infection in the absence of CD4$^+$ T cells. Our results also show that BCG/BCG::ESAT-6-PE25SS vaccination-mediated reduction, and in some cases even prevention of *Mtb* dissemination, is a consequence of the repositioning of CD8$^+$ T cells and B cells at the edge of lymphatic lesions. While the role of B cells is unclear and they appear to be passive bystanders, CD8$^+$ T cells actively promote LTBI containment in the infected LNs rather than via preferential killing in the lung.

It has previously been shown that in certain situations, B cells can contribute to the immune response against *Mtb* via antibody and cytokine production as antigen-presenting cells and through their contributions to the formation of granulomas[47]. Surprisingly, the absence of mature B cells in B6.*muMT*$^{-/-}$ mice did not lead to *Mtb* dissemination nor the premature death of infected mice. In fact, B6.*muMT*$^{-/-}$ mice showed almost no signs of a productive infection with *Mtb* at all. While these results support previous studies that reported that B cells are either not required to control TB or promote detrimental effects[48,49], they also contradict others in which B cells and antibodies played an important role in TB immunity[50–52]. It is increasingly clear that the role of B cells in TB is context- and animal-model dependent[47,53]. The findings obtained in our study imply that B cells are either actively attracted and exploited by *Mtb* to establish an early, productive infection in the LNs, or that B cells are predominantly needed to help T cell localisation within the granuloma. This hypothesis is supported by results from an elegant study showing that *Mtb* infection leads to a massive influx of B cells into the lung draining mediastinal LNs, which limits protective T cell activation[54]. It is also conceivable that the expansion of B cells seen in the LNs after CD4$^+$ T cell depletion is simply a consequence of the increase in antigen and cell-free *Mtb* bacilli after the breakdown of the granuloma[55].

Upon dissemination of lymphatic *Mtb* with anti-CD4 mAb we observed a strong neutrophil degranulation signature. Given that neutrophilia is a common response to bacterial infections[40], the degranulation signature likely reflects the granuloma breakdown and increased bacterial burden associated with the anti-CD4 mAb-mediated granuloma disruption[56]. Very recently, it has also been shown that antibodies with distinct Fc variants could restrict *Mtb* growth via a neutrophil-dependent pathway[57]. It is also known that B cells regulate neutrophilia during *Mtb* infection and BCG vaccination[58]. Given that our spatial transcriptomics results highlighted both neutrophil degranulation as well as B cell responses as the top hits associated with *Mtb* dissemination, it is possible that B cell-neutrophil interactions can also further amplify *Mtb* infection in the lymphatics. It is also conceivable that the increase in lymphatic B cells and neutrophils serves as a host compensatory mechanism to overcome CD4$^+$ T cell depletion. Alternatively, B cell expansion could also help to direct T follicular-like

https://doi.org/10.1038/s41467-026-70911-4

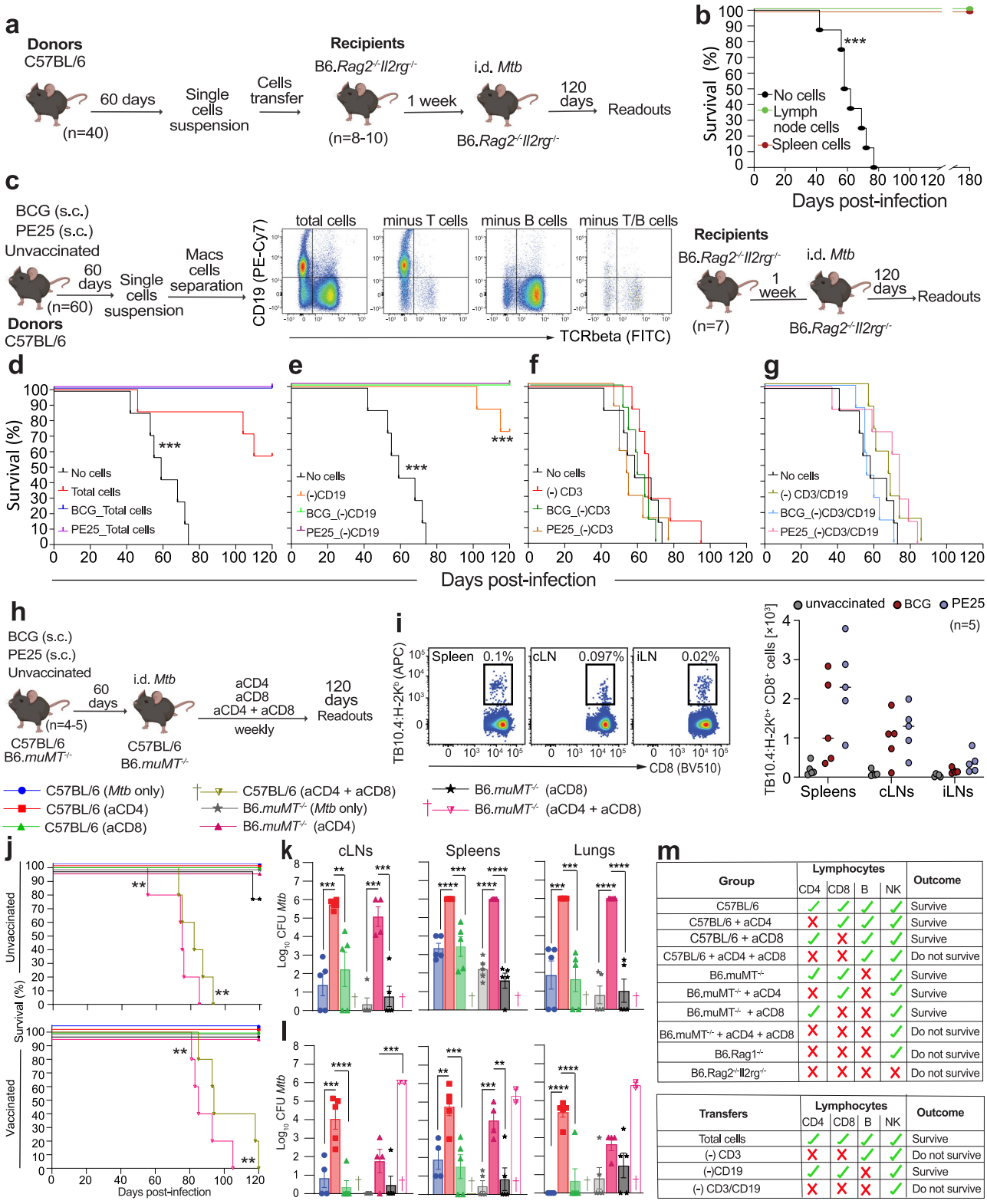

helper cells into lymphoid follicles, as has recently been shown following aerosol *Mtb* infection[59].

The use of genetic deficiency of T, B or NK cells, combined with adoptive transfer experiments into lymphocyte deficient B6.*Rag2*$^{-/-}$*Il2rg*$^{-/-}$ mice, showed that vaccine-mediated containment of *Mtb* in the lymphatics following depletion of CD4$^+$ T cells is driven by adaptive immunity, with a very minor (if any) contribution of innate immune mechanisms. In particular, our data support a model whereby CD4$^+$ T cell deficiency is compensated for by CD8$^+$ T cells. It has previously been shown that the reactivation of latent pulmonary TB induced by antibiotic therapy in mice is exacerbated when CD8$^+$ T cells are depleted[60]. It is also known that CD8$^+$ T cells can maintain the balance between *Mtb* control and the prevention of excessive tissue damage during LTBI[61].

This work makes it increasingly clear that CD8$^+$ T cell immunity should be induced by a successful TB vaccine. Our results show that BCG vaccination leads to a repositioning of CD8$^+$ T cells around *Mtb* bacilli in infected LNs, which prevents bacterial escape from the lesion.

Fig. 6 | CD8⁺ T cells mediate LTBI containment following immunosuppression and B cells are dispensable. a Experimental setup of mice receiving adoptive cell transfer (Recipients) from spleen and LNs derived from naïve C57BL/6 mice (Donors, $n = 40$). Recipients: No cells $n = 8$, Lymph node cell $n = 8$, Spleen cells $n = 10$). **b** Percent survival of B6.*Rag2*$^{-/-}$*Il2rg*$^{-/-}$ mice following i.d. infection with *Mtb* that have received either LN cells, spleen cells, or no cells from naïve donors. **c** Experimental setup for adoptive transfer from unvaccinated and vaccinated mice (Donors), including representative FACS plots of LN cells following depletion of T cells, B cells, or both. **d**–**g** Percent survival of B6.*Rag2*$^{-/-}$*Il2rg*$^{-/-}$ mice (Recipients) following i.d. infection with *Mtb* that have received either total LN cells (**d**), B cell-depleted LN cells (**e**), T cell-depleted LN cells (**f**), or B and T cell-depleted LN cells (**g**) from naïve donors or BCG or PE25-vaccinated donors. Each group contains 7 mice ($n = 7$) (**d**–**g**). **h** Experimental setup of C57BL/6 and B6.*muMT*$^{-/-}$ mice treated weekly with anti-CD4 mAb, anti-CD8 mAb or both anti-CD4 and anti-CD8 mAb. **i** TB10.4:H-2K^{b+}CD8⁺ cells in spleen, cLN and inguinal lymph nodes (iLN) following vaccination with BCG or PE25. **j** Survival of C57BL/6 and B6.*muMT*$^{-/-}$ treated with anti-CD4 mAb, anti-CD8 mAb or both anti-CD4 and anti-CD8 mAb. **k**, **l** CFU in cLNs, spleens and lungs at 120 days following i.d. *Mtb* infection. **m** Table summarising the survival results of all wild-type and knockout mice with and without immunosuppression via mAb-mediated cell depletion (top). Table summarising the survival results of B6.*Rag2*$^{-/-}$*Il2rg*$^{-/-}$ mice receiving total LN cells, or T cell, B cell or T and B cell-depleted LN cells (bottom). Results are presented as survival means (**b-g, j**), representative FACS plots (**c**, **i**) and individual data points ± SEM. $n = 40$–60 donor and 7–10 recipient mice (**i**, **k**, **l**) and $n = 5$ (B6.*muMT*$^{-/-}$=4) (**j**, **k**, **l**). Representative images from 2 pooled independent experiments with similar results (**b**, **c**, **d**–**g**). Statistical analyses: One-way ANOVA followed by Tukey's multiple comparison test (one-sided) (**k**, **l**) and Long-rank (Mantel-Cox) test (two-sided) for survival curves (**b**–**g**, **j**). Significant differences are indicated by asterisks: * $p_{HSD} < 0.05$ (**i**), ** $p_{PHT} < 0.01$ (**k**, **l**), *** $p_{HSD\_PHT} < 0.001$(**d**, **e**, **k**, **l**), **** $p_{PHT} < 0.0001$(**k**, **l**). † indicates mortality. Gating strategy shown in Fig. S8. Source data are provided as a Source Data file. The mouse icon is from BioRender. Kupz, A. (https://BioRender.com/65s841b).

Given that the expansion of CD8⁺ T cell numbers was only minor, it is likely that CD8⁺ T cell-dependent bacterial control is a consequence of altered functionality. These results provide further support for the development of vaccines that directly target CD8⁺ T cell-driven immune responses. Very recently, it has been shown that CD4⁺ T cells and CD8α⁺ lymphocytes, but not CD8αβ T cells, are crucial for the near-sterile protection offered by intravenous BCG vaccination in non-human primates[62]. The results point towards a unique, non-redundant role for CD4⁺ and CD8α⁺ lymphocytes, with depletion of either cell type leading to increased *Mtb* bacterial load in the lungs. Given that we used a CD8α targeting anti-CD8 mAb clone (2.43), and CD8α depletion affects both adaptive and innate-like immune cells, including NK cells and MAIT cells, it is possible that innate-like CD8⁺ cell subsets may also play a role in our model. Although *Rag*-deficient mice lack αβ-positive T cells[43], and *Rag*-deficient mice phenocopied the lethal *Mtb* dissemination seen with anti-CD8/anti-CD4 mAb treatment, further studies should investigate the precise contribution of CD8α⁺ vs CD8αβ⁺ cells in reactivation of LTBI, and also how these cells mediate their effector functions.

Our study also provides novel insights into the reactivation dynamics of lymphatic LTBI across a spectrum of organ systems. It appears that anti-CD4 mAb-mediated reactivation of LTBI affects not only multiple peripheral lymphatic sites, such as the cervical and mesenteric LNs and the spleen but also the liver and the bone marrow. Interestingly, BCG vaccination prevented histopathological changes associated with *Mtb* dissemination in all those affected sites. However, how translatable are those findings to human LTBI? Epidemiological data suggest that BCG vaccination has limited efficacy in preventing human LTBI reactivation[63,64]. It is, however, important to note that LTBI reactivation in humans predominantly happens in adults, especially in the elderly and after immunosuppression, often many decades after BCG vaccination. As such, it will be important to understand if the immune mechanisms that mediate prevention of LTBI reactivation in this murine model are long-lived. Although recent clinical trials did not show beneficial effects of BCG revaccination in adults for the prevention of sustained *Mtb* infection[65], it remains to be investigated if BCG revaccination in adults can prevent LTBI reactivation in older age. Our findings also provide hope that vaccination-induced CD8⁺ T cell-mediated immune responses can be incorporated into TB vaccines for use in HIV co-infected individuals.

Our study also has limitations. Firstly, while this model of contained *Mtb* infection is now widely accepted as a useful model to mimic LTBI[17,18,66], it uses an i.d. inoculation, a route that is not the cause of human LTBI. It will be useful to investigate if CD8⁺ T cells also mediate containment of LTBI in other animal models and in humans. As mentioned above, it will also be critical to dissect if the protective effect is attributable to CD8αα-expressing T cell subsets, as well as innate-like cells. For that reason, depletion studies utilising different mAb clones should be conducted. Furthermore, it remains to be investigated if CD8⁺ cells functionally mediate the containment of LTBI via specific soluble mediators or direct killing. Our findings also show that there was no outstanding improvement in the containment of LTBI when a rBCG strain was used. In some instances the response of BCG::ESAT-6-PE25SS was even inferior to BCG, despite the increased antigenic repertoire in BCG::ESAT-6-PE25SS. It is known that the secretion of ESAT-6 leads to additional immune activation and the perforation of the phagosomal membrane. Whether this leads to specific immune- or stromal cell alterations in the cLNs with implications for *Mtb* containment remains to be investigated. Similarly, although we experimentally confirmed the expression of functional *Mtb* ESAT-6 by our rBCG strain, the amount of ESAT-6 required, and its cytoplasmic sustainability in APCs to induce a persistent immune activation in vaccinated animals were not explored. Thus, further detailed analysis of optimal ESAT-6 levels and the kinetics of immune activation at different ESAT-6 levels in APCs are warranted to optimize the immunogenicity and/or protective efficacy of our rBCG. However, given that most rBCGs only differ from BCG in a very small number of antigens, our study implies that the mechanisms of vaccination-mediated containment are largely driven by factors that are shared between BCG and rBCGs. Future studies should investigate which components of BCG drive containment and if containment can also be induced by subunit TB vaccine candidates.

Finally, while we have attempted to utilise multiple high-resolution histopathological and imaging approaches, we did not perform single cell resolved spatial transcriptomics. Mature single cell spatial platforms were only emerging when this study began, and future studies should endeavour to use single cell transcriptomic resolution for better integration with histological techniques for maximum resolution[67,68]. The use of single cell spatial transcriptomics will also allow future studies to further differentiate effector functions of CD8⁺ T cells associated with natural vs vaccination-mediated containment, and provide information about a potential role for moonlighting, as has been described in a NHP model of TB[69].

In conclusion, we provide direct evidence of CD8⁺ T cell-mediated control of LTBI in immunocompromised hosts and question the role of B cells in lymphatic *Mtb* containment. We also provide a detailed atlas and a transcriptomic resource for lymphatic *Mtb* infection with and without prior vaccination. Our findings have profound implications for the understanding of immunity to TB more broadly and the management of LTBI. The robust model of controlled LTBI reactivation used here may also be relevant to gain further detailed insights into the cellular dynamics after *Mtb* dissemination across a spectrum of different organs.

Methods

Bacterial cultures

The BCG SSI (abbreviated to BCG; ATCC no. 35733) and BCG::ESAT-6-PE25SS[41], (abbreviated to PE25 in Figures) and *Mtb* H37Rv strains were

cultured in Middlebrook 7H9 broth enriched with 10% Albumin Dextrose Catalase (ADC) (Cat. No. 271310 and 212352, respectively, Becton, Dickinson and Company (BD)), 0.2% glycerol (Cat. No. AJA242, Ajax Finechem), and 0.05% Tween 80 (vol/vol) (Cat. No. 822187, Sigma-Aldrich). BCG::ESAT-6-PE25SS and *Mtb* H37Rv were grown in the presence of 50 μl/ml kanamycin and 10 μl/ml ampicillin, respectively. The cultures were shaken at 80-90 rpm at 37 °C until they reached the log phase with an OD_{600} of 0.6-0.8. The bacterial cultures were then harvested, washed, aliquoted in 10% glycerol and kept at -80°C until use.

Mice

Six- to eight-week-old female C57BL/6 (C57BL/6JOzarc; JAX stock #000664) mice were obtained from the Animal Resources Centre (ARC) Perth, WA, Australia. Male and female C57BL/6, B6.*muMT*$^{-/-}$ (JAX stock #002288)[42], B6.*Rag1*$^{-/-}$ (B6.129S7-Rag1^{tm1Mom}/Arc; JAX stock #002216)[43] and B6.*Rag2*$^{-/-}$*Il2rg*$^{-/-}$ (JAX stock #014593)[44] mice were bred and maintained in specific pathogen-free conditions at the James Cook University Bioresource Facility of the Australian Institute of Tropical Health and Medicine (AITHM) in Townsville, QLD, Australia. Experimental and control animals were co-housed, and before performing experiments, the animals were acclimatised to the facility for at least seven days. The mouse rooms were maintained with a 12-hour light/dark cycle, a temperature of 21 ± 2 °C, and a humidity of 55% ± 10%. The mice were housed in ventilated cages with bedding consisting of irradiated fine corn cobs, enriched with a cardboard roll, Bed R Nest, cotton, and some pieces of wood for them to chew. Water was treated by reverse osmosis and sterilised by UV light. The irradiated mouse diet was obtained from Specialty Feeds (WA, Australia). Both food and water were provided ad libitum. All experimental procedures were approved by the Animal Welfare and Ethics Committee of James Cook University (approval number A2794). Each mouse was monitored for clinical signs of disease and/or weighed throughout the study.

Vaccinations and infections

Mice were immunised via s.c. injection in the base of the tail with 100 μl of phosphate buffer saline (PBS) (Cat. No. 10010023, Gibco) containing 1×10^6 CFU of BCG or BCG::ESAT-6-PE25SS. Sixty days after vaccination, with an i.p. injection of anti-CD4 (aCD4) mAb (clone GK1.5; 200 μg/mouse; Walter and Eliza Hall Institute of Medical Research (WEHI) antibody facility) or anti-CD8 (aCD8) mAb (clone 2.43; 200 μg/mouse; WEHI antibody facility) (Table S1) and infected (i.d.) in the ear with 1×10^3 CFU of *Mtb*. aCD4 and aCD8 antibody injections continued weekly for the duration of the experiment. Naïve, vaccination-only, immunosuppressed-only, and infection-only groups were included as controls. The experimental setup is shown in the Figures. Samples were collected at 30, 60, and 120 days after *Mtb* infection.

Disease indicator score

The clinical signs of disease for immunisations, immunosuppression and infections in C57BL/6, B6.*muMT*$^{-/-}$, B6.*Rag1*$^{-/-}$ and B6.*Rag2*$^{-/-}$*Il2rg*$^{-/-}$ mice were scored from 0 to 3 according to approved animal ethics project A2794 as follows: a) Appearance: 0 = Shiny fur, clear eyes, 1 = Fur appears untended with or without a lesion in the skin, 2 = Scruffy fur, discharge from eyes and nose, eyes sunken and anus dirty or sore, 3 = Very scruffy fur, blood from orifices, abnormal body posture; b) Behaviour/movement: 0 = Normal contact with other mice, active movement, 1 = Little contact with other mice, 2 = Little contact with other mice, avoid movement, 3 = Complete isolation, noises, self-harm, no-movement, lying on side; c) Reaction to stimuli: 0 = Adequate, 1 = Slightly delayed, 2 = Significantly delayed or weak, 3 = No reaction; d) Breathing: 0 = Normal; 1 = Increased breathing, 2 = Increased breathing with sporadic increase in abdominal breathing, 3 = Constant abdominal breathing; and e) Weight loss: 0 = None, 1 = Less than 10%, 2 = 10% to 14%, 3 = ≥ 15%. Mice were euthanised by cervical dislocation by trained and experienced staff when they reached a score of 3 on any criterion.

Sample collection

Mice were euthanised by cervical dislocation and spleens, cLNs and right lung lobes were collected for *Mtb* CFU enumeration. mLNs, lungs, brains, salivary glands, livers, femurs, cLNs, and left lung lobes were fixed in 4% paraformaldehyde for 24 hours. After being fixed, the samples were transferred into 70% ethanol until they were processed for histopathological studies.

CFU enumeration

Spleens, cLNs and lungs were homogenised in Nasco Whirl-Pak bags or gentleMACS tubes containing 1 ml of PBS enriched with 0.05% Tween 80. Tenfold dilutions (N, -1, -2) were plated onto Middlebrook 7H11 (Cat. No. 212203, BD) agar plates supplemented with 0.2% glycerol, 0.05% Tween 80, 10% oleic albumin dextrose catalase (OADC) (Cat. No. 212240, BD), 25 μl/ml ampicillin and 10 μl/ml cycloheximide (Cat. No. A9518 and C7698, respectively, Merk). Agar plates were sealed, wrapped in aluminium foil, and incubated aerobically at 37°C, and CFU were counted after four weeks.

Histopathological studies

Tissue samples were embedded in paraffin and sectioned into 4-micrometre-thick slices. Slices were transferred onto microscope slides, dewaxed, and stained using the following methods:

Hematoxylin and Eosin (H&E). mLNs, brains, salivary glands, livers, femurs, cLNs, and left lung lobes were stained with H&E. Briefly, dewaxed tissues were hydrated, stained with hematoxylin, differentiated, blued, and then stained with Eosin. Subsequently, the tissues were dehydrated, cleared, and cover-slipped before analysis. Scoring of H&E slides was performed blinded.

Ziehl-Neelsen (ZN). mLNs, brains, salivary glands, livers, femurs, cLNs, and left lung lobes were stained with ZN. In brief, dewaxed tissues were hydrated, stained with Carbol Fuchsin, Ziehl-Neelsen, and differentiated in acid alcohol. Afterwards, tissues were counterstained with methylene blue, dehydrated in ethyl alcohol, cleared, and cover-slipped before analysis.

9-colour Opal Immunohistochemistry (IHC). cLNs and left lung lobes were stained with a 9-colour Opal IHC Multiplex panel (Akoya) by the Advanced Histotechnology Facility of the WEHI, Melbourne, Victoria, Australia. The 9-colour Opal IHC panel included the following antibodies: *Mtb* (Cat. No. ab905, clone pAb, Abcam), CD3 (Cat. No. A045229-2, clone pAb, Dako), CD4 (Cat. No. 14-9766-82, clone 4SM95, Invitrogen), CD8a (Cat. No. HS361-008, clone Rb321E9, Synaptic systems), B220 (Cat. No. 103202, clone RA3-6B2, Biolegend)), CD161c/NK1.1 (Cat. No. 24395S, clone E6Y9G, Cell Signalling Technology), CD11c (Cat. No. 97585, clone D1V9Y, Cell Signalling Technology), CD11b (Cat. No. ab133357, clone EPR1344, Abcam), and Spectral DAPI (Cat. No. FP1490, Akoya Bioscience).

Whole Transcriptome Analysis (WTA). cLNs were stained using the NanoString GeoMx Mouse Whole Transcriptome Assay (version 3.0.0.182) by NanoString Technologies, Inc. (Seattle, Washington, USA). Thirty regions of interest (ROIs) were selected based on areas with different histopathological changes seen in H&E. ROIs were derived from 8 mice per experimental group and from 2 naïve controls, and included three areas: I) Normal in Naïve = no pathological changes in mice that did not receive treatment, and Normal in disease = no pathological changes were seen in tissues from *Mtb*-only infected mice, immunosuppressed and *Mtb*-infected, and vaccinated-

immunosuppressed and *Mtb*-infected; II) Lesion = tissue resembling granuloma; and III) Edge of the Lesion = border of the tissue resembling granuloma.

Digital image analysis

Tissues stained with H&E and ZN were scanned at 20× and 40× using the PhenoImager HT (Akoya) and the Aperio LV1 (Leica Biosystems), respectively, while the Multiplex IHC slides were scanned using the PhenoImager HT (Akoya) at 20×. QuPath versions 3.1-5.1 were used to analyse H&E, ZN and Multiplex IHC slides. Each LN and lung lobe were selected for the three different staining techniques. The areas affected by *Mtb* were identified, and their respective percentages were calculated for H&E. In the ZN staining, *Mtb* were identified, and the proportion of the area occupied by the bacteria was calculated. In the multiplex IHC, cell nuclei were identified using DAPI before cellular segmentation. Subsequently, two methodologies were applied. Briefly, each cell was determined by a threshold and classified according to the marker expressed by a threshold, and subsequently, multiple markers were used to train a machine-learning classification of the cell types for each cell. Once each cell was classified according to its phenotype, cells were enumerated, and distances among cells were analysed[70]. Cellular deconvolution and counts for estimating the abundance of cell types within each ROI were performed using the GeoMx DSP Analysis Suite. The analysis utilised the DSPPlugSpatialDecon and the scripting file SpatialDecon_plugin.R alongside the cell profile metrics ImmuneAtlas_cellFamily_ImmGen.

Cell isolation and adoptive transfer

Spleen and LNs were collected aseptically from naïve and vaccinated C57BL/6 donor mice. The tissues were dissociated using a sterile three cc syringe plunger and passed through a 70µm cell strainer. Red cells were lysed using red cell lysis buffer.

To deplete $CD3^+$ and/or $CD19^+$ cells prior to adoptive cell transfer, LNs were disrupted as described above. The cell separation was carried out using the CD3e MicroBead kit and CD19 MicroBeads (Miltenyi Biotec). Briefly, single-cell suspensions were labelled with CD3- or CD19-conjugated immunomagnetic beads and then depleted using a MACS system (Miltenyi Biotec). Further enrichment was achieved by passing the negative fraction through a second MACS column. Flow cytometry analysis showed that ~90–98% of $CD3^+$ (CD3-FITC; clone 17A2; Cat. No. 555274; BD Biosciences) and/or $CD19^+$ (CD19-PE-Cy7; clone ID3; Cat. No. 552854; BD Biosciences) cells were effectively removed.

For adoptive transfer experiments[71], B6.*Rag2*$^{-/-}$*Il2rg*$^{-/-}$ recipient mice received 5.7×10^5 to 7×10^6 cells via intravenous (i.v.) injection into the tail vein. The recipient mice were infected with *Mtb* i.d. 1-7 days after cell transfer.

Flow cytometry

Identification of mycobacteria-specific $CD8^+$ T cells was performed by using antibodies against CD3-A700 (clone 500 A2; Cat. No. 557984), CD4-PerCP-Cy5.5 (clone RM 4-5; Cat. No. 55094), CD8-BV510 (clone 53-6.7; Cat. No. 563068) and CD44-BV421 (clone IM7; Cat. No. 563970); all purchased from BD Biosciences. Monomers of H-2K^b *Mtb* TB10.4 4-11 IMYNYPAM were provided by the NIH Tetramer Core Facility, USA. Monomers were tetramerized with Streptavidin-APC (Agilent Technologies) in house, according to NIH Tetramer Core Facility instructions. Single cells were incubated with Fixable Viability stain 780 (BD Biosciences) for 10 minutes at room temperature and washed with FACS buffer solution. Samples were then incubated with the H-2Kb *Mtb* TB10.4 tetramer (1:50 dilution) for 1 hour at room temperature and washed with FACS buffer solution. Cells were then incubated for 30 minutes with surface antibodies (1:200 dilution) on ice and washed with FACS buffer solution. Samples were resuspended in 150 µl of blank calibration particles 6.0–6.4 µm (BD Biosciences) diluted in FACS buffer solution (1:74) for subsequent enumeration. Samples were analysed using a FACSCanto-II or FortessaX20 analyser (BD Biosciences) (Table S1).

RNA sequencing from fixed cervical lymph nodes

RNA extraction, library preparation, sequencing and initial data processing were performed by Lexogen NGS Services, Lexogen GmbH, Austria. In brief, RNA from cLNs was isolated using PureLink FFPE RNA Isolation Kit (ThermoFisher). Samples were characterized by UV-Vis spectrophotometry (Nanodrop2000c, Thermo Fisher) and RNA integrity was assessed on a Fragment Analyser System using the DNF-471 RNA Kit (15 nt) (Agilent). To remove genomic DNA contaminants, the samples were treated with DNase I. The libraries were constructed using Lexogen's QuantSeq 3′ mRNA-Seq Library Prep Kit FWD. Prepared libraries were quality controlled on a Fragment Analyser System using the DNF-474 and the HS-DNA kit (1-6000 bp) (Agilent). cDNA libraries were sequenced with an Illumina NextSeq 2000 platform using 100 nt single end read length, with 5 million reads on average per sample.

Sequencing quality control of the raw reads was assessed using FastqQC software, and adapter sequences were removed with cutadapt[72]. Alignment to the *Mus musculus* reference genome (GRCm38, Ensembl release 102) and read counting were performed using STAR[73] and featureCounts[74]. The DESeq2 R package[75] was used to perform differential gene expression analysis.

Oligonucleotides for library synthesis including the first strand oligo(dT) primer, second strand synthesis random primers, and library amplification primers are propitiatory to Lexogen. Illumina sequencing primers are available on page 27 of the Lexogen QuantSeq user guide-(https://www.lexogen.com/wp-content/uploads/2023/07/191UG444V0111_QuantSeq_FWD_UDI_V2_Kits_2023-07-12.pdf).

Data analysis & statistics

Data analysis was performed using different software: GraphPad Prism versions 9.3.1 to 10.6.1; R and RStudio version 4.3.1. R packages included NanoStringNCTools, GeomxTools, GeoMxWorkflows and GeoMx-NGS gene panel version Mm_R_NGS_WTA_v1.0. For image analysis and representative images, QuPath versions v0.3.1 to v0.5.0, Image J version 1.53 and GIMP versions 2.10.30 to 2.10.36 were used. The significance of DEGs in the volcano plots was determined using a false discovery cut-off rate (FDR) < 0.05. The Venn diagrams were plotted using significant DEGs for each comparison with the VennDiagram package in R. The pathway analyses were done using the QIAGEN Ingenuity pathway analysis (IPA) version 24.0.2. Flow cytometry data was collected using BD FACSDiva software and analysed using FlowJo version 10.8.1 Results are presented as data means ± SEM. Statistical comparisons were performed using Mann-Whitney test, One-way ANOVA with Kruskal-Wallis test with Dunn's multiple comparison test, or Long-rank (Mantel-Cox) test Two-way ANOVA with Tukey's multiple comparison test and Fisher's exact test. Data were considered significant when $^*p < 0.05$, $^{**}p < 0.01$, $^{***}p < 0.001$, $^{****}p < 0.0001$.

Reporting summary

Further information on research design is available in the Nature Portfolio Reporting Summary linked to this article.

Data availability

All data are included in the Supplementary Information or available from the authors, as are unique reagents used in this Article. The raw numbers for charts and graphs are available in the Source Data file whenever possible. The NanoString GeoMx data generated in this study have been deposited in the GEO repository under accession code GSE314979. The RNA sequencing data generated in this study have been deposited in the GEO database under accession code GSE320238. Source data are provided with this paper.

Code availability

This paper does not report original codes. Any additional information required to reanalyse the data reported in this paper is available in the main text and supplemental information or from the lead contact upon request.

References

1. WHO. Global Tuberculosis Report 2024. http://www.who.int/tb/publications/global_report/en/ (2024).
2. Muñoz, P., Rodríguez, C. & Bouza, E. Mycobacterium tuberculosis infection in recipients of solid organ transplants. *Clin. Infect. Dis.* **40**, 581–587 (2005).
3. El-Sadr, W. M. & Tsiouris, S. J. HIV-associated tuberculosis: diagnostic and treatment challenges. *Semin Respir. Crit. Care Med* **29**, 525–531 (2008).
4. Crampin, A. C. et al. Recurrent TB: relapse or reinfection? the effect of HIV in a general population cohort in Malawi. *Aids* **24**, 417–426 (2010).
5. Winter, J. R. et al. The impact of HIV infection on tuberculosis transmission in a country with low tuberculosis incidence: a national retrospective study using molecular epidemiology. *BMC Med.* **18**, 385 (2020).
6. McShane, H. Insights and challenges in tuberculosis vaccine development. *Lancet Resp. Med.* **7**, 810–819 (2019).
7. Gengenbacher, M. & Kaufmann, S. H. Mycobacterium tuberculosis: success through dormancy. *FEMS Microbiol Rev.* **36**, 514–532 (2012).
8. Nunes-Alves, C. et al. In search of a new paradigm for protective immunity to TB. *Nat. Rev. Microbiol.* **12**, 289–299 (2014).
9. Behr, M. A. & Waters, W. R. Is tuberculosis a lymphatic disease with a pulmonary portal? *Lancet Infect. Dis.* **14**, 250–255 (2014).
10. Kupz, A., Zedler, U., Staber, M. & Kaufmann, S. H. A mouse model of latent tuberculosis infection to study intervention strategies to prevent reactivation. *PLoS One* **11**, e0158849 (2016).
11. Hühns, M., Erbersdobler, A., Obliers, A. & Röpenack, P. Identification of HPV types and mycobacterium tuberculosis complex in historical long-term preserved formalin fixed tissues in different human organs. *PLoS One* **12**, e0170353 (2017).
12. González-Escalada, A., Rebollo, M. J., Barrios Payan, J., HernáNdez-pando, R. & García, M. J. Detection of mycobacterial dna in human bone marrow. *Microorganisms* https://doi.org/10.3390/microorganisms11071788 (2023).
13. Holty, J. E., Gould, M. K., Meinke, L., Keeffe, E. B. & Ruoss, S. J. Tuberculosis in liver transplant recipients: a systematic review and meta-analysis of individual patient data. *Liver Transpl.* **15**, 894–906 (2009).
14. Pribula, V., Bodnár, J. & Vrzgula, A. Liver Tuberculosis a case report. *Rozhl. Chir.* **97**, 394–398 (2018).
15. Thada, P. K. et al. in *StatPearls* (StatPearls Publishing Copyright © 2024, StatPearls Publishing LLC., 2024).
16. Duffy, F. J. et al. Use of a contained mycobacterium tuberculosis mouse infection model to predict active disease and containment in humans. *J. Infect. Dis.* **225**, 1832–1840 (2022).
17. Mai, D. et al. Exposure to mycobacterium remodels alveolar macrophages and the early innate response to mycobacterium tuberculosis infection. *PLoS Pathog.* **20**, e1011871 (2024).
18. Nemeth, J. et al. Contained *Mycobacterium tuberculosis* infection induces concomitant and heterologous protection. *PLoS Pathog.* **16**, e1008655 (2020).
19. Sathkumara, H. D. et al. BCG Vaccination Prevents Reactivation of Latent Lymphatic Murine Tuberculosis Independently of CD4+ T Cells. *Front. Immunol.* https://doi.org/10.3389/fimmu.2019.00532 (2019).
20. Malik, A. A., Sinha, S., Ehtesham, N. Z. & Hasnain, S. E. End tuberculosis by 2035: challenges ahead. *Future Microbiol* **18**, 461–464 (2023).
21. Moore, S. C., Anderson, S. J. & Walker, W. S. Mouse macrophages contain a truncated CD4 transcript. *J. Leukoc. Biol.* **52**, 128–129 (1992).
22. Cohen, S. B. et al. Alveolar macrophages provide an early mycobacterium tuberculosis niche and initiate dissemination. *Cell Host Microbe* **24**, 439–446.e434 (2018).
23. Flynn, J. L., Chan, J. & Lin, P. L. Macrophages and control of granulomatous inflammation in tuberculosis. *Mucosal Immunol.* **4**, 271–278 (2011).
24. Feria, M. G. et al. Pro-inflammatory alterations of circulating monocytes in latent tuberculosis infection. *Open Forum Infect. Dis.* **9**, ofac629 (2022).
25. Dries, R. et al. Advances in spatial transcriptomic data analysis. *Genome Res* **31**, 1706–1718 (2021).
26. Sawyer, A. J. et al. Spatial mapping reveals granuloma diversity and histopathological superstructure in human tuberculosis. *J. Exp. Med.*https://doi.org/10.1084/jem.20221392 (2023).
27. Liu, Y. M. et al. Combined single-cell and spatial transcriptomics reveal the metabolic evolvement of breast cancer during early dissemination. *Adv. Sci. (Weinh.)* **10**, e2205395 (2023).
28. Wang, F. et al. Single-cell and spatial transcriptome analysis reveals the cellular heterogeneity of liver metastatic colorectal cancer. *Sci. Adv.* **9**, eadf5464 (2023).
29. Du, Y. et al. Integration of pan-cancer single-cell and spatial transcriptomics reveals stromal cell features and therapeutic targets in tumor microenvironment. *Cancer Res* **84**, 192–210 (2024).
30. Schäbitz, A. et al. Spatial transcriptomics landscape of lesions from non-communicable inflammatory skin diseases. *Nat. Commun.* **13**, 7729 (2022).
31. Flores-Valdez, M. A., Kupz, A. & Subbian, S. Recent Developments in Mycobacteria-Based Live Attenuated Vaccine Candidates for Tuberculosis. *Biomed.* https://doi.org/10.3390/biomedicines10112749 (2022).
32. Singh, A. K., Srikrishna, G., Bivalacqua, T. J. & Bishai, W. R. Recombinant BCGs for tuberculosis and bladder cancer. *Vaccine* **39**, 7321–7331 (2021).
33. Lewis, K. N. et al. Deletion of RD1 from Mycobacterium tuberculosis mimics bacille Calmette-Guerin attenuation. *J. Infect. Dis.* **187**, 117–123 (2003).
34. Gröschel, M. I. et al. Recombinant BCG expressing ESX-1 of mycobacterium marinum combines low virulence with cytosolic immune signaling and improved TB protection. *Cell Rep.* **18**, 2752–2765 (2017).
35. Heijmenberg, I. et al. ESX-5-targeted export of ESAT-6 in BCG combines enhanced immunogenicity & efficacy against murine tuberculosis with low virulence and reduced persistence. *Vaccine* **39**, 7265–7276 (2021).
36. Baykan, A. H. et al. Extrapulmonary tuberculosıs: an old but resurgent problem. *Insights into Imaging* **13**, 39 (2022).
37. García-Pérez, B. E., Mondragón-Flores, R. & Luna-Herrera, J. Internalization of Mycobacterium tuberculosis by macropinocytosis in non-phagocytic cells. *Micro. Pathog.* **35**, 49–55 (2003).
38. Li, Q., Wang, J., Zhang, M., Tang, Y. & Lu, H. Discovery of CD3(+) CD19(+) cells, a novel lymphocyte subset with a potential role in human immunodeficiency virus-Mycobacterium tuberculosis coinfection, using mass cytometry. *Clin. Transl. Med* **11**, e681 (2021).
39. Ramon-Luing, L. A. et al. Mycobacterium tuberculosis H37Rv Strain Increases the Frequency of CD3(+)TCR(+) Macrophages and Affects Their Phenotype, but Not Their Migration Ability. *Intl. J. Mol. Sci.*https://doi.org/10.3390/ijms23010329 (2021).
40. Tahir, N. & Zahra, F. in *StatPearls* (StatPearls Publishing Copyright © 2024, StatPearls Publishing LLC., 2024).
41. Gern, B. H. et al. Early and opposing neutrophil and CD4 T cell response shape pulmonary tuberculosis pathology, *J. Exp. Med.* **222**, e20250161 (2025).

42. Kitamura, D., Roes, J., Kuhn, R. & Rajewsky, K. A B cell-deficient mouse by targeted disruption of the membrane exon of the immunoglobulin [mu] chain gene. *Nature* **350**, 423–426 (1991).
43. Mombaerts, P. et al. RAG-1-deficient mice have no mature B and T lymphocytes. *Cell* **68**, 869–877 (1992).
44. Mazurier, F. et al. A novel immunodeficient mouse model-RAG2 x common cytokine receptor gamma chain double mutants-requiring exogenous cytokine administration for human hematopoietic stem cell engraftment. *J. Interferon Cytokine Res.* **19**, 533–541 (1999).
45. Wang, J., Fan, X. Y. & Hu, Z. Immune correlates of protection as a game changer in tuberculosis vaccine development. *NPJ vaccines* **9**, 208 (2024).
46. Houben, R. M. G. J. & Dodd, P. J. The Global Burden of Latent Tuberculosis Infection: A Re-estimation Using Mathematical Modelling. *PLOS Med.* **13**, e1002152 (2016).
47. Stewart, P. et al. Role of B Cells in Mycobacterium Tuberculosis Infection. *Vaccines (Basel)* https://doi.org/10.3390/vaccines11050955 (2023).
48. Chen, Y. et al. B cells promote granulomatous inflammation during chronic Mycobacterium tuberculosis infection in mice. *PLOS Pathog.* **19**, e1011187 (2023).
49. Bosio, C. M., Gardner, D. & Elkins, K. L. Infection of B cell-deficient mice with CDC 1551, a clinical isolate of Mycobacterium tuberculosis: delay in dissemination and development of lung pathology. *J. Immunol.* **164**, 6417–6425 (2000).
50. Tsai, C.-Y. et al. Splenic marginal zone B cells restrict Mycobacterium tuberculosis infection by shaping the cytokine pattern and cell-mediated immunity. *Cell rep.*https://doi.org/10.1016/j.celrep.2024.114426 (2024).
51. Lu, L. L. et al. A Functional Role for Antibodies in Tuberculosis. *Cell* **167**, 433–443.e414 (2016).
52. Maglione, P. J., Xu, J. & Chan, J. B cells moderate inflammatory progression and enhance bacterial containment upon pulmonary challenge with Mycobacterium tuberculosis. *J. Immunol.* **178**, 7222–7234 (2007).
53. Chan, J. et al. The role of B cells and humoral immunity in Mycobacterium tuberculosis infection. *Semin. Immunol.* **26**, 588–600 (2014).
54. Daniel, L. et al. Stromal structure remodeling by B lymphocytes limits T cell activation in lymph nodes of Mycobacterium tuberculosis-infected mice. *J. Clin. Invest.* https://doi.org/10.1172/jci157873 (2022).
55. Rao, M. et al. B in TB: B cells as mediators of clinically relevant immune responses in tuberculosis. *Clin. Infect. Dis.: Off. Publ. Infect. Dis. Soc. Am.* **61**, S225–S234 (2015).
56. Stadthagen, G. et al. Genetic basis for the biosynthesis of methylglucose lipopolysaccharides in Mycobacterium tuberculosis. *J. Biol. Chem.* **282**, 27270–27276 (2007).
57. Irvine, E. B. et al. Fc-engineered antibodies promote neutrophil-dependent control of Mycobacterium tuberculosis. *Nat. Microbiol.* https://doi.org/10.1038/s41564-024-01777-9 (2024).
58. Kozakiewicz, L. et al. B cells regulate neutrophilia during Mycobacterium tuberculosis infection and BCG vaccination by modulating the interleukin-17 response. *PLoS Pathog.* **9**, e1003472 (2013).
59. Swanson, R. V. et al. Antigen-specific B cells direct T follicular-like helper cells into lymphoid follicles to mediate Mycobacterium tuberculosis control. *Nat. Immunol.* **24**, 855–868 (2023).
60. van Pinxteren, L. A., Cassidy, J. P., Smedegaard, B. H., Agger, E. M. & Andersen, P. Control of latent Mycobacterium tuberculosis infection is dependent on CD8 T cells. *Eur. J. Immunol.* **30**, 3689–3698 (2000).
61. Lin, P. L. & Flynn, J. L. CD8 T cells and Mycobacterium tuberculosis infection. *Semin Immunopathol.* **37**, 239–249 (2015).
62. Simonson, A. W. et al. Intravenous BCG-mediated protection against tuberculosis requires CD4+ T cells and CD8α+ lymphocytes. *J. Exp. Med.*https://doi.org/10.1084/jem.20241571 (2025).
63. Huang, W. et al. The effect of BCG vaccination and risk factors for latent tuberculosis infection among college freshmen in China. *Int J. Infect. Dis.* **122**, 321–326.322 (2022).
64. Andersen, P. & Doherty, T. M. The success and failure of BCG - implications for a novel tuberculosis vaccine. *Nat. Rev. Microbiol* **3**, 656–662 (2005).
65. Schmidt, A. C. et al. BCG revaccination for the prevention of Mycobacterium tuberculosis infection. *N. Engl. J. Med.* **392**, 1789–1800 (2025).
66. Cohen, S. B. et al. Host and pathogen genetic diversity shape vaccine-mediated protection to Mycobacterium tuberculosis. *Front Immunol.* **15**, 1427846 (2024).
67. Tan, X. et al. A robust platform for integrative spatial multi-omics analysis to map immune responses to SARS-CoV-2 infection in lung tissues. *Immunology* **170**, 401–418 (2023).
68. Tu, W. J. et al. In vivo inhibition of nuclear ACE2 translocation protects against SARS-CoV-2 replication and lung damage through epigenetic imprinting. *Nat. Commun.* **14**, 3680 (2023).
69. Winchell, C. G. et al. CD8+ lymphocytes are critical for early control of tuberculosis in macaques. *J. Exp. Med.*https://doi.org/10.1084/jem.20230707 (2023).
70. Bankhead, P. et al. QuPath: Open source software for digital pathology image analysis. *Sci. Rep.* **7**, 16878 (2017).
71. Kupz, A. et al. ESAT-6–dependent cytosolic pattern recognition drives noncognate tuberculosis control in vivo. *J. Clin. Invest.*https://doi.org/10.1172/JCI84978 (2016).
72. Martin, M. Cutadapt removes adapter sequences from high-throughput sequencing reads. *EMBnet. J.* **17**, 10–12 (2011).
73. Dobin, A. et al. STAR: ultrafast universal RNA-seq aligner. *Bioinforma. (Oxf., Engl.)* **29**, 15–21 (2013).
74. Liao, Y., Smyth, G. K. & Shi, W. featureCounts: an efficient general purpose program for assigning sequence reads to genomic features. *Bioinforma. (Oxf., Engl.)* **30**, 923–930 (2014).
75. Love, M. I., Huber, W. & Anders, S. Moderated estimation of fold change and dispersion for RNA-seq data with DESeq2. *Genome Biol.* **15**, 550 (2014).

Acknowledgements

We thank Serrin Rowarth, Kylie Robertson, Bradley Taylor, and Olivia Johnson for their support in the Animal Facility. We thank Erin Roberts, and Roselfina Charol for their assistance in the Histopathology Department, and Leanne Taylor for support with BSL3 work. We thank the NIH Tetramer facility for providing H-2K^{b} *Mtb* TB10.4 4-11 IMYNYPAM monomers. This study was funded by NIH grant R01AI161822 to S.S and A.K. The NHMRC Ideas Grant (APP2001262) and Investigator Grant (APP2008715) supported the laboratory of A.K. NHMRC Investigator Grant (APP5121190) supported M.A.F. The funders were not involved in the study design, data collection and the decision to submit the article for publication.

Author contributions

Conceptualisation: S.M.H., S.S., A.K. Methodology: S.M.H., M.K., A.H., E.G., X.T., J.T., M.T.M., Z.C., L.P.R., M.D., M.R., M.A.F.V., A.B., Q.N., S.S., M.A.F., A.K. Investigation: S.M.H., M.K., A.H., E.G., X.T., J.T., M.T.M., Z.C.C., L.D.P., Y.P., E.T., M.L.D., M.E.R., M.A.F.V., A.B., Q.N., S.S., M.A.F., A.K. Manuscript writing: S.M.H., A.K. Manuscript editing: S.M.H., M.K., A.H., E.G., X.T., J.T., M.T.M., Z.C., L.P.R., Y.P., E.T., M.L.D., M.E.R., M.A.F.V., A.B., Q.N., S.S., M.A.F., A.K. Funding acquisition: S.S., M.A.F., A.K.

Competing interests

A.K. is an inventor on the patent "Recombinant strains of *Mycobacterium bovis* BCG" issued to James Cook University. M.A.F.V. is an inventor in

patent "BCG vaccine strains protecting against the establishment of latent mycobacterium tuberculosis infection". The other authors declare no competing interests.

Additional information

Supplementary information The online version contains supplementary material available at (https://doi.org/10.1038/s41467-026-70911-4).

Correspondence and requests for materials should be addressed to Andreas Kupz.

Peer review information *Nature Communications* thanks the anonymous reviewer(s) for their contribution to the peer review of this work. A peer review file is available.

Reprints and permissions information is available at http://www.nature.com/reprints

Publisher's note Springer Nature remains neutral with regard to jurisdictional claims in published maps and institutional affiliations.

[1]Australian Institute of Tropical Health and Medicine, James Cook University, Townsville and Cairns, Qld, Australia. [2]Centre for Tropical Bioinformatics and Molecular Biology, Australian Institute of Tropical Health and Medicine, James Cook University, Cairns, Qld, Australia. [3]UQ Centre for Clinical Research, The University of Queensland, Brisbane, Qld, Australia. [4]eResearch Centre, James Cook University, Townsville, Qld, Australia. [5]Institute for Molecular Bioscience, The University of Queensland, and QIMR Berghofer Medical Research Institute, Brisbane, Qld, Australia. [6]College of Science and Engineering, James Cook University, Townsville, Qld, Australia. [7]Brain & Mental Health Program, QIMR Berghofer Medical Research Institute, Brisbane, Qld, Australia. [8]School of Biomedical Sciences, Faculty of Health, Medicine and Behavioural Sciences, The University of Queensland, Brisbane, Qld, Australia. [9]Advanced Histotechnology Facility, Walter and Eliza Hall Institute of Medical Research, Parkville, Vic, Australia. [10]Frazer Institute, The University of Queensland, Translational Research Institute, Brisbane, Qld, Australia. [11]Centro de Investigación y Asistencia en Tecnología y Diseño del Estado de Jalisco (CIATEJ), A.C., Biotecnología Médica y Farmacéutica, Guadalajara, Jal, Mexico. [12]Public Health Research Institute (PHRI), New Jersey Medical School, Rutgers University, Newark, NJ, USA. [13]These authors contributed equally: Manoharan Kumar, Alec Henderson, Erin Graham. [14]These authors jointly supervised this work: Selvakumar Subbian, Matt A. Field, Andreas Kupz. ✉e-mail: andreas.kupz@jcu.edu.au